

Watermass co-ordinates isolate the historical ocean warming signal

Taimoor Sohail¹, R M Holmes², and J D Zika¹

¹University of New South Wales

²University of Sydney

December 7, 2022

Abstract

Persistent warming and water cycle change due to anthropogenic climate change modifies the temperature and salinity distribution of the ocean over time. This ‘forced’ signal of temperature and salinity change is often masked by the background internal variability of the climate system. Analysing temperature and salinity change in watermass-based coordinate systems has been proposed as an alternative to traditional Eulerian (e.g., fixed-depth, zonally-averaged) co-ordinate systems. The impact of internal variability is thought to be reduced in watermass co-ordinates, enabling a cleaner separation of the forced signal from background variability - or a higher ‘signal-to-noise’ ratio. Building on previous analyses comparing Eulerian and water-mass-based one-dimensional coordinates, here we recast two-dimensional co-ordinate systems - temperature-salinity (? - ?), latitude-longitude and latitude-depth - onto a directly comparable equal-volume framework. We compare the internal variability, or ‘noise’ in temperature and salinity between these remapped two-dimensional co-ordinate systems in a 500 year pre-industrial control run from a CMIP6 climate model. We find that the median internal variability is lowest (and roughly equivalent) in ? - ? and latitude-depth space, compared with latitude-longitude co-ordinates. A large proportion of variability in ? - ? and latitude-depth space can be attributed to processes which operate over a timescale greater than 10 years. Overall, the signal-to-noise ratio in ? - ? co-ordinates is roughly comparable to latitude-depth co-ordinates, but is greater in regions of high historical temperature change. Conversely, latitude-depth co-ordinates have greater signal-to-noise ratio in regions of historical salinity change. Thus, we conclude that the climatic temperature change signal can be more robustly identified in watermass-co-ordinates.

1 **Watermass co-ordinates isolate the historical ocean warming signal**

2 T. Sohail^{a,b}, R. M. Holmes^c and J.D. Zika^{a,b,d}

3 ^a *School of Mathematics and Statistics, University of New South Wales, Sydney, Australia*

4 ^b *Australian Centre for Excellence in Antarctic Science (ACEAS), University of New South Wales,*
5 *NSW, Australia*

6 ^c *School of Geosciences, University of Sydney, Sydney, Australia*

7 ^d *UNSW Data Science Hub, University of New South Wales, Sydney, Australia*

8 *Corresponding author: Taimoor Sohail, t.sohail@unsw.edu.au*

9 ABSTRACT: Persistent warming and water cycle change due to anthropogenic climate change
10 modifies the temperature and salinity distribution of the ocean over time. This ‘forced’ signal
11 of temperature and salinity change is often masked by the background internal variability of the
12 climate system. Analysing temperature and salinity change in watermass-based coordinate systems
13 has been proposed as an alternative to traditional Eulerian (e.g., fixed-depth, zonally-averaged)
14 co-ordinate systems. The impact of internal variability is thought to be reduced in watermass
15 co-ordinates, enabling a cleaner separation of the forced signal from background variability - or
16 a higher ‘signal-to-noise’ ratio. Building on previous analyses comparing Eulerian and water-
17 mass-based one-dimensional coordinates, here we recast two-dimensional co-ordinate systems -
18 temperature-salinity ($T - S$), latitude-longitude and latitude-depth - onto a directly comparable
19 equal-volume framework. We compare the internal variability, or ‘noise’ in temperature and
20 salinity between these remapped two-dimensional co-ordinate systems in a 500 year pre-industrial
21 control run from a CMIP6 climate model. We find that the median internal variability is lowest
22 (and roughly equivalent) in $T - S$ and latitude-depth space, compared with latitude-longitude co-
23 ordinates. A large proportion of variability in $T - S$ and latitude-depth space can be attributed
24 to processes which operate over a timescale greater than 10 years. Overall, the signal-to-noise
25 ratio in $T - S$ co-ordinates is roughly comparable to latitude-depth co-ordinates, but is greater in
26 regions of high historical temperature change. Conversely, latitude-depth co-ordinates have greater
27 signal-to-noise ratio in regions of historical salinity change. Thus, we conclude that the climatic
28 temperature change signal can be more robustly identified in watermass-co-ordinates.

29 SIGNIFICANCE STATEMENT: Changes in ocean temperature and salinity are driven both by
30 human-induced climate change and by modes of natural variability in the climate system, such as
31 the El-Niño Southern Oscillation. It can be difficult to isolate the human-induced ‘signal’ of climate
32 change from the natural fluctuations or ‘noise’ in the climate system. Watermass-based methods,
33 which ‘follow’ a parcel of water around the ocean, have been thought to improve on ‘Eulerian’
34 (i.e., analyses performed at fixed latitude, longitude and depth) frames of reference as they are
35 less impacted by the ‘noise’. However, it is difficult to cleanly compare between watermass-based
36 methods and Eulerian methods. Here, we aim to quantify the extent to which watermass-based
37 frameworks improve on Eulerian frameworks in isolating the climate signal from the noise. We
38 recast watermass and Eulerian methods onto an equivalent grid, enabling a clean comparison
39 between them, and find that doing so increases the signal-to-noise ratio in watermass-based co-
40 ordinates in regions of ocean warming. These results emphasise the utility of watermass-based
41 methods in analysing long-term climatic temperature change in the ocean.

42 **1. Introduction**

43 Anthropogenic climate change is characterised by the persistent build-up of heat in the climate
44 system (Stocker et al. 2013) and long-term changes to the hydrological cycle (Durack et al. 2012;
45 Sohail et al. 2022). A vast proportion of excess heat in the climate system is absorbed by the
46 ocean (Schuckmann et al. 2020), and changes to the water cycle manifest as ocean salinity changes
47 (Pierce et al. 2012). These human-induced changes to ocean heat and salinity occur alongside
48 natural variability in the climate system, driven in part by physical modes of climate variability
49 like the El-Niño Southern Oscillation (ENSO) (Trenberth 2020) and the North Atlantic Oscillation
50 (Visbeck et al. 2001). Natural variability in the climate system can obscure forced anthropogenic
51 trends in the ocean, adding ‘noise’ to the signal.

52 Numerous studies have aimed to tackle the problem of detecting the anthropogenic signal of
53 climate change in observations and climate models. A conventional approach to detecting changes
54 in ocean temperature and/or salinity involves detecting changes to ocean properties at fixed loca-
55 tions on the ocean surface (that is, in latitude-longitude co-ordinates, Hawkins and Sutton 2012;
56 Hamlington et al. 2011) or by zonally-averaging (that is, in latitude-depth co-ordinates, Pierce et al.
57 2012; Boyer et al. 2005; Swart et al. 2018; Hobbs et al. 2021). In these traditional Eulerian frames

58 of reference, the ‘noise’, natural variability in the climate system, can be reduced by coarsening
59 the grid, filtering out the relevant time-scales, taking large ensemble means, and/or by focusing
60 on specific ocean regions that may not be impacted by dominant modes of variability (Hamling-
61 ton et al. 2011; Penland and Matrosova 2006; Maher et al. 2021; Pierce et al. 2012). In doing
62 so, past research has effectively increased the ‘signal-to-noise’ ratio - allowing for a more robust
63 identification of the long-term climate change-induced trend.

64 Watermass-based frameworks have been proposed as an alternative to traditional Eulerian-based
65 methods for tracking ocean change. Tracking changes in ocean properties following iso-surfaces
66 of conservative tracers, such as density, temperature and/or salinity, is thought to filter out short-
67 timescale, highly variable adiabatic motions, potentially reducing internal variability and noise
68 in the system (Silvy et al. (2020); Palmer et al. (2007); Zika et al. (2015, 2021)). In addition,
69 watermass-based methods can enable a direct attribution of heat or salt content tendencies to
70 surface fluxes and diabatic mixing, as only diabatic flux terms are present in the budget (Walin
71 1982; Groeskamp et al. 2019; Holmes et al. 2019; Bladwell et al. 2021; Hieronymus et al. 2014).

72 However, a clean comparison of the internal variability, and thus signal-to-noise ratio, in
73 watermass-based and Eulerian methods is challenging because the volume bounded by watermass-
74 based coordinate surfaces can change with time. Thus, a given temperature or salinity surface could
75 expand to fill a large portion of the ocean, while volumes bounded by latitude, longitude and depth
76 surfaces are (by construction) fixed in time. For instance, Palmer et al. (2007); Palmer and Haines
77 (2009) compared ocean temperature variability above the 14°C isotherm, and the 220m depth
78 level, which are approximately geographically collocated. While the use of a temperature-based
79 co-ordinate reduces internal variability, the 14°C isotherm expands over time to accommodate an
80 increasingly warm ocean, while the 220m depth level remains fixed. Following work by Sohail
81 et al. (2021), Holmes et al. (2022) avoided this problem by using a percentile-based co-ordinate
82 system that enables a constant-volume comparison between one-dimensional temperature, depth
83 and latitude co-ordinate systems. Holmes et al. (2022) showed that internal variability is indeed
84 reduced in one-dimensional temperature co-ordinates (aligning with findings from Palmer and
85 Haines (2009)), but only for specific timescales and regions of the ocean.

86 While one-dimensional fixed-depth and fixed-temperature frameworks remain popular choices
87 in assessing ocean heat and salt content (Wolfe et al. 2008; Morrison and Hogg 2013; Sohail et al.

88 2021, 2022), two-dimensional co-ordinate systems retain more information and are often used
89 to assess ocean heat and salt content change (e.g., Roemmich et al. (2015); Silvy et al. (2020);
90 Rathore et al. (2020)). For instance, in one dimension, ‘cold’ temperature surfaces conflate the
91 ocean interior with surface polar regions, but introducing a second dimension (e.g. salinity) isolates
92 the interior ocean from the polar surface effectively. Variability in two-dimensional watermass
93 coordinates has been compared to variability in Eulerian coordinates by ‘re-projecting’ diabatic
94 tendencies inferred in water mass coordinates back onto the geographical coordinates. Evans
95 et al. (2014) inferred seasonal diabatic tendencies in Temperature versus Salinity (hereafter $T - S$)
96 co-ordinates within the Drake Passage and then remapped these onto the average locations of the
97 corresponding $T - S$ classes along a repeat hydrographic section. Similarly, Zika et al. (2021)
98 inferred the diabatic tendencies necessary to explain changes in the global inventories of sea water
99 in $T - S$ coordinates and mapped these onto the 3D geographical distribution of those water masses.
100 In each case, Eulerian changes were larger than the inferred diabatic tendencies. However, these
101 methods have relied on inferring the diabatic tendency from either a numerical model or an inverse
102 model, and the derived solution is not necessarily unique. Thus, a clean, objective comparison
103 assessing whether the projection of internal variability into two-dimensional watermass frameworks
104 (e.g. $T - S$ co-ordinates) is reduced compared to Eulerian counterparts (e.g., latitude-longitude,
105 latitude-depth) has not been conducted.

106 In this paper, we recast two dimensional co-ordinate systems, namely, $T - S$ space, latitude-
107 longitude space, and latitude-depth space, onto a constant-volume-based two-dimensional frame-
108 work using a statistical method called *Binary Space Partitioning* (BSP). We then track changes
109 to the ocean’s temperature and salinity properties to quantify the internal variability (the ‘noise’)
110 with the aim of establishing whether the signal-to-noise ratio of the climate signal increases in
111 watermass-based frameworks. The coupled climate model data used in this study is described
112 in section 2. We provide details of BSP and its two-dimensional remapping in section 3. Our
113 findings, detailed in section 4, confirm that the median internal variability (the ‘noise’) is lowest
114 in $T - S$ and latitude-depth space, and is described by longer timescale processes. We explore the
115 historical ‘signal’ in section 5, and show that signal-to-noise ratio is larger in $T - S$ space in regions
116 of high temperature change compared to its Eulerian counterparts. Conclusions are summarised
117 in section 6.

118 2. Model data: ACCESS-CM2

119 In this work, we focus on a number of simulations performed using the ACCESS-CM2 climate
120 model (Bi et al. 2020) as part of the Australian submission to the 6th generation Climate Model
121 Intercomparison Project (CMIP6) (Eyring et al. 2016). The ocean model component of ACCESS-
122 CM2 is the Modular Ocean Model version 5.1 (Griffies and Greatbatch 2012) and uses Conservative
123 Temperature and Practical Salinity as its standard temperature and salinity variables (McDougall
124 2003; McDougall and Barker 2011). More details on ACCESS-CM2, the ACCESS-CM2 submis-
125 sion to CMIP6, and in particular, the forcing and spin-up of the piControl and historical runs, are
126 provided by Bi et al. (2020); Mackallah et al. (2022).

127 We analyse a 500 year pre-industrial control (piControl) simulation, as well as a 165 year
128 historical simulation (Eyring et al. 2016). In this work, we analyse the model Potential Temperature,
129 Practical Salinity and grid cell volume variables in temperature-salinity, latitude-longitude, and
130 latitude-depth coordinates over the entire pre-industrial control period, and the entire historical
131 period, covering 1850 to 2014. A single ensemble member (*r1i1p1f1*) is used in this analysis.

132 The monthly-averaged temperature and salinity in the piControl and historical runs are first
133 binned into 2D $T - S$, latitude-longitude and latitude-depth percentile coordinates using BSP as
134 described in section 3. As in Irving et al. (2020), we find that the pre-industrial control simulation
135 has a persistent drift in both temperature and salinity. The globally-integrated heat content grows
136 significantly (by $O(10^{24})$ J) over the 500-year period of the control run, while the ocean freshwater
137 flux drops by $O(10^{16})$ kg. In order to remove these long-term drifts in the pre-industrial control
138 run, we de-drift and de-season binned outputs. De-drifting is accomplished by removing a cubic
139 fit of the piControl time series over the relevant overlapping time period, following Irving et al.
140 (2020). The seasonal cycle is removed by subtracting the time-mean seasonal cycle over the entire
141 time period of interest from the monthly time series.

142 Note that de-drifting and de-seasoning is conducted *after* aggregating or reorganising data into its
143 relevant diagnostic. This is primarily because removing the drift from every grid point in the native
144 grid does not guarantee there will be no drift in the aggregated or reorganised data. De-drifting
145 after binning ensures that any drift in the system is removed in the final diagnostic, and thus does
146 not contaminate calculations of variance in this diagnostic.

147 3. Theory

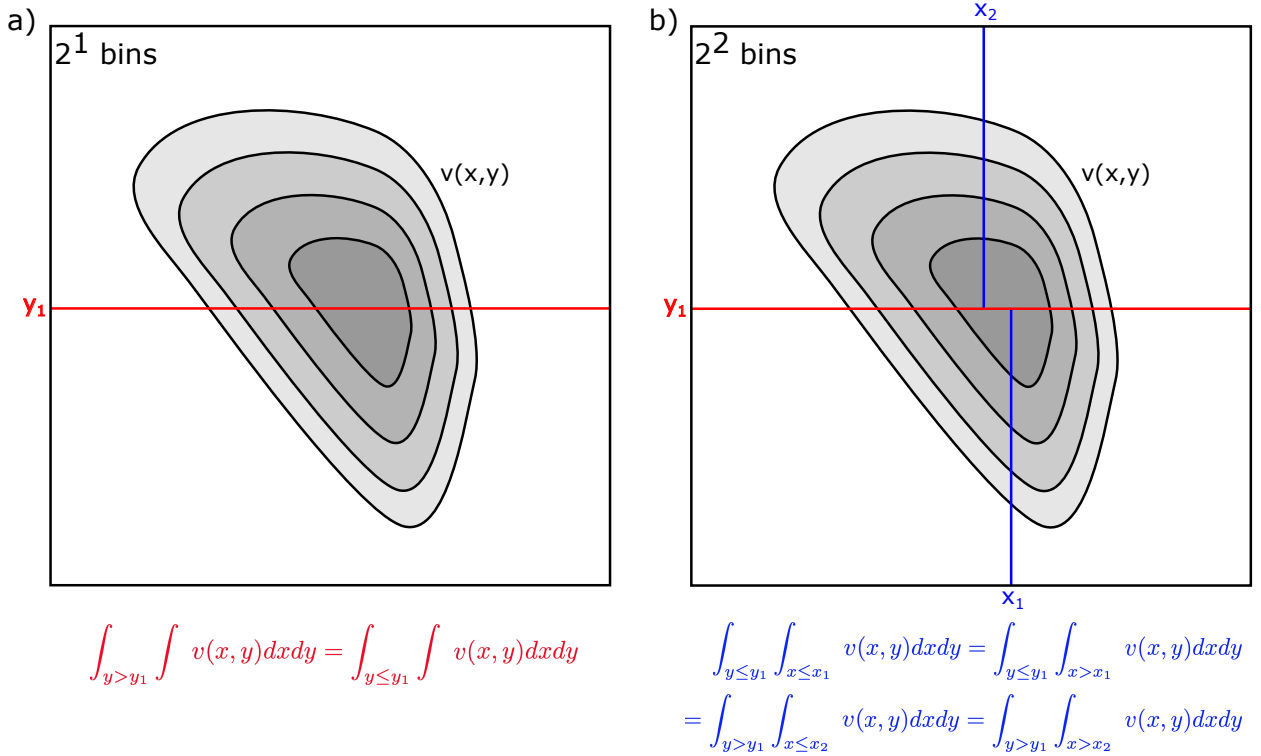
148 Typically, watermass-based analyses involve tracking ocean properties at constant temperature
149 or salinity (Worthington 1981; Walin 1982; Zika et al. 2015, 2018; Holmes et al. 2019). By
150 following constant tracer isosurfaces, the heat and salt budgets contain contributions from diabatic
151 processes only. However, there are still diasurface volume fluxes in these coordinates which must
152 be accounted for and whose associated tracer flux may be ill-defined (see Holmes et al. (2019) and
153 Bladwell et al. (2021) for details). In addition, as the surface outcrop location of temperature and
154 salinity surfaces may shift over time, it is difficult to link changes at a given tracer isosurface to a
155 specific geographical region in strongly forced ocean models. Thus, cleanly comparing between
156 pure watermass-based coordinate systems and Eulerian coordinate systems (which track ocean
157 changes at fixed latitude, longitude or depth) can be difficult, in part because Eulerian coordinate
158 systems are fixed-volume by construction, while the volume of water bounded by temperature or
159 salinity surfaces can change with time.

160 *a. Binary Space Partitioning*

161 In order to overcome this issue, we recast all 2D co-ordinate systems using a statistical method
162 called Binary Space Partitioning (BSP). Originating from computer graphics and image processing
163 fields (e.g. Radha et al. (1996); Thibault and Naylor (1987)), BSP is a method for recursively,
164 hierarchically subdividing a distribution using arbitrarily oriented lines. We can use BSP to
165 effectively partition the ocean's two-dimensional volume distribution into equal weight bins in
166 watermass and Eulerian space.

167 To illustrate how BSP works, consider a two-dimensional volume distribution $v(x, y)$ which is
168 the volume of sea-water per unit x and y . x and y can be coordinates defined by Eulerian space
169 or coordinates defined by time variable scalars such as T, S, density, etc. To form a BSP tree, we
170 recursively subdivide the distribution with alternating axis-oriented lines n times, such that the
171 volume of the ocean in each subdivision is $1/2^n$ of the total ocean volume $\iint v(x, y) dx dy$. This
172 procedure is shown graphically in Figure 1.

173 The initial slice (figure 1a) divides the volume in half along some y -value y_1 , such that each
174 subdivision contains half of the ocean volume $\frac{1}{2} \iint v(x, y) dx dy$. The subsequent slice (figure
175 1b) divides each subdivided section further in half along two x -values x_1 and x_2 , such that each

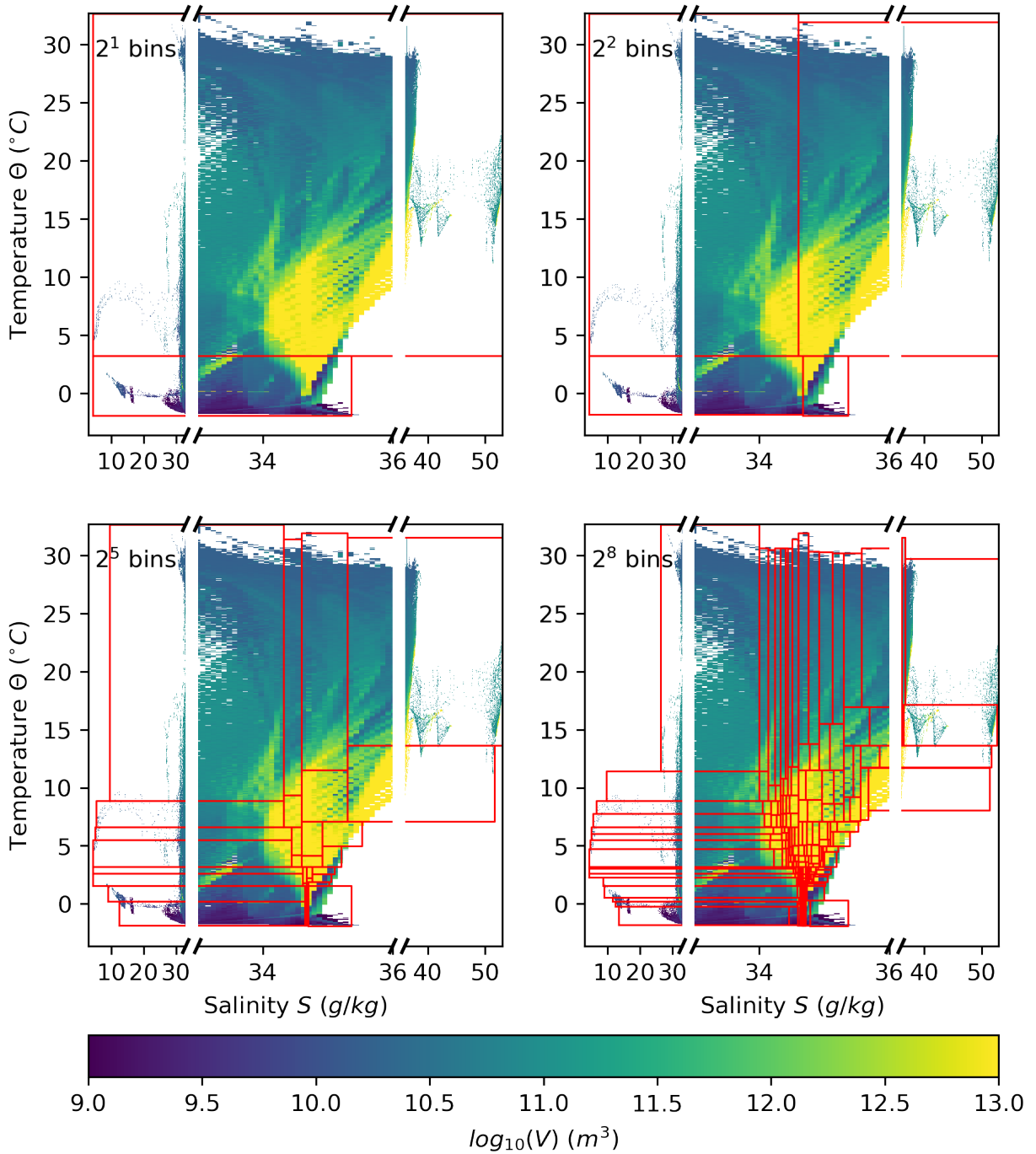


184 FIG. 1. A simple demonstration of Binary Space Partitioning applied to a generic two-dimensional volume
 185 distribution. a) One slice orthogonal to the y -axis at y_1 (in red) yields 2^1 equal-volume bins of $v(x, y)$. b) Two
 186 additional slices orthogonal to the x -axis at x_1, x_2 (in blue) yield 2^2 equal-volume bins of $v(x, y)$.

176 subdivision now contains a quarter of the ocean volume, $\frac{1}{4} \iint v(x, y) dx dy$. This process of recursive
 177 subdivision is repeated n times along alternating axes such that each time a volume constraint of
 178 $\frac{1}{2^n} \iint v(x, y) dx dy$ is met. The resulting BSP tree structure thus compresses any general distribution
 179 into equal-volume bins.

180 Once the BSP has been performed for a given choice of x and y coordinates, we can track changes
 181 to the mean temperature, T and salinity, S in each bin over time. This allows us to quantify how
 182 variability (‘noise’) behaves in each co-ordinate system regardless of whether it is Eulerian or
 183 water-mass based.

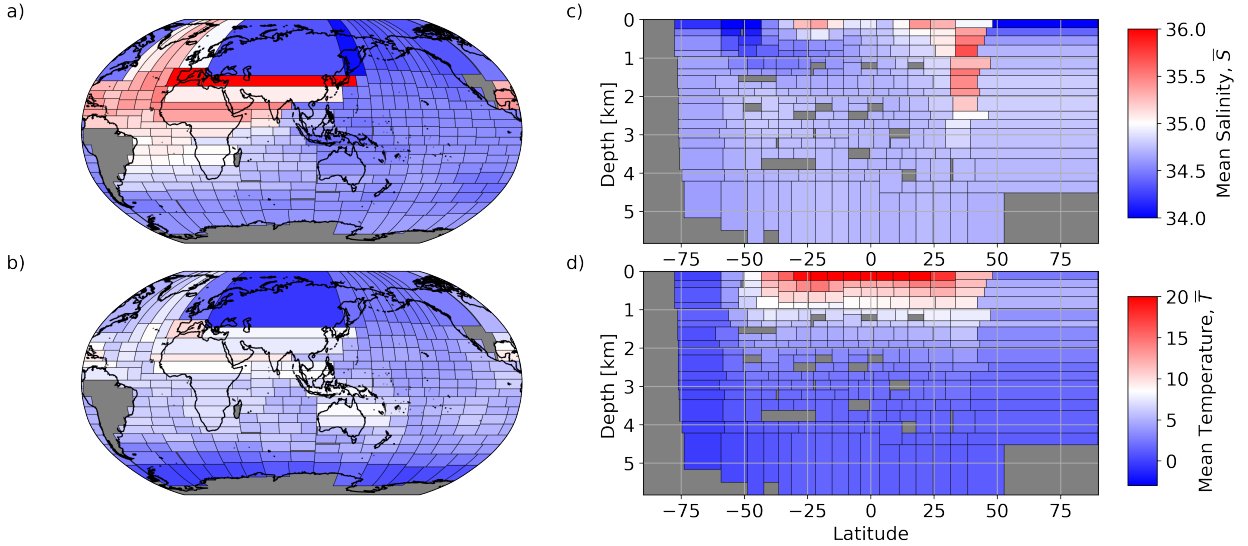
187 In this work, we use BSP to partition the ocean’s volume into 2^n equal-volume bins in three
 188 2D coordinate systems: $T - S$, latitude-longitude and latitude-depth space. We first illustrate the
 189 partitioning of the ocean’s $T - S$ volume distribution in the ACCESS-CM2 piControl run in figure
 190 2 for $n = 1, 2, 5$, and 8.



191 FIG. 2. BSP splitting on alternating axes, applied to the time-mean ACCESS-CM2 piControl volumetric
 192 distribution in $T-S$ space, with 2^n bins, where a) $n=1$, b) $n=2$, c) $n=5$, and d) $n=8$. Note that the salinity axis
 193 has three linear scales, delineated by the two horizontal breaks.

194 In latitude-longitude and latitude-depth co-ordinates, we perform BSP on the depth-integrated
195 and zonally-integrated time-mean volume distribution, respectively. Figure 3 shows the resulting
196 BSP bins in both Eulerian co-ordinate systems for $n = 8$, coloured by their mean temperature and
197 salinity. The BSP binning algorithm only ‘sees’ the (depth- or zonally-integrated) ocean volume,
198 ignoring any land masses. The BSP algorithm will thus not abide by continental boundaries and it
199 will form bins that stretch across continents and between ocean basins to meet the equal volume
200 constraint. To limit such inter-basin BSP bins, and to account for the periodicity of longitude, we
201 choose to ensure that the Americas and Drake Passage form both the far western and far eastern
202 boundary of the ocean. This is done by slicing the ocean at 70°W longitude from 90°S to 3°N
203 latitude. Then, a diagonal slice is made from 70°W longitude to 100°W between 3°N latitude and
204 20°N , and the slice continues north from 20°N to 90°N along the 100°W longitude. Data points
205 between this line and the Greenwich Meridian, moving east, are labelled with negative longitudes
206 (i.e. are measured west of Greenwich) while the remaining data points to the east of Greenwich are
207 labeled with positive longitudes (i.e. are measured east of Greenwich). This ensures, for example,
208 that data points either side of the Isthmus of Panama do not combine into the same BSP bin (hence
209 the grey, empty cells in figure 3a and b)

210 The BSP algorithm dynamically adjusts its bin limits to capture equal volumes at all times.
211 In a time-varying vertical grid modeling system (as in ACCESS-CM2 which uses a z^* vertical
212 coordinate), this dynamic adjustment, combined with grid cell volume changes in coarse-resolution
213 regions, can lead to an unphysical representation of model properties. Specifically, in the coarsely-
214 resolved deep ocean, infinitesimal fluctuations in the grid cell volume due to the movements of
215 the coordinate system surfaces can trigger large changes in BSP bin limits. This means that the
216 deep ocean variability can appear to be quite large within a given BSP bin, driven primarily by
217 changing bin limits as they accommodate small volumetric changes in sparsely resolved regions of
218 the ocean. The impact of the coarse vertical resolution on the BSP binning algorithm is clear in
219 figure 3c and d, where empty regions are scattered through depth amongst the BSP bins. This is
220 because, as the model grid coarsens vertically, the volume, T and S information becomes aligned
221 along increasingly distant grid cell centers. Hence, the BSP algorithm needs to make a decision
222 about which grid cells to cover to ensure a set of equal-volume bins. This leads to some regions
223 not being covered by any BSP bins, as they do not contain any model information (grey cells in

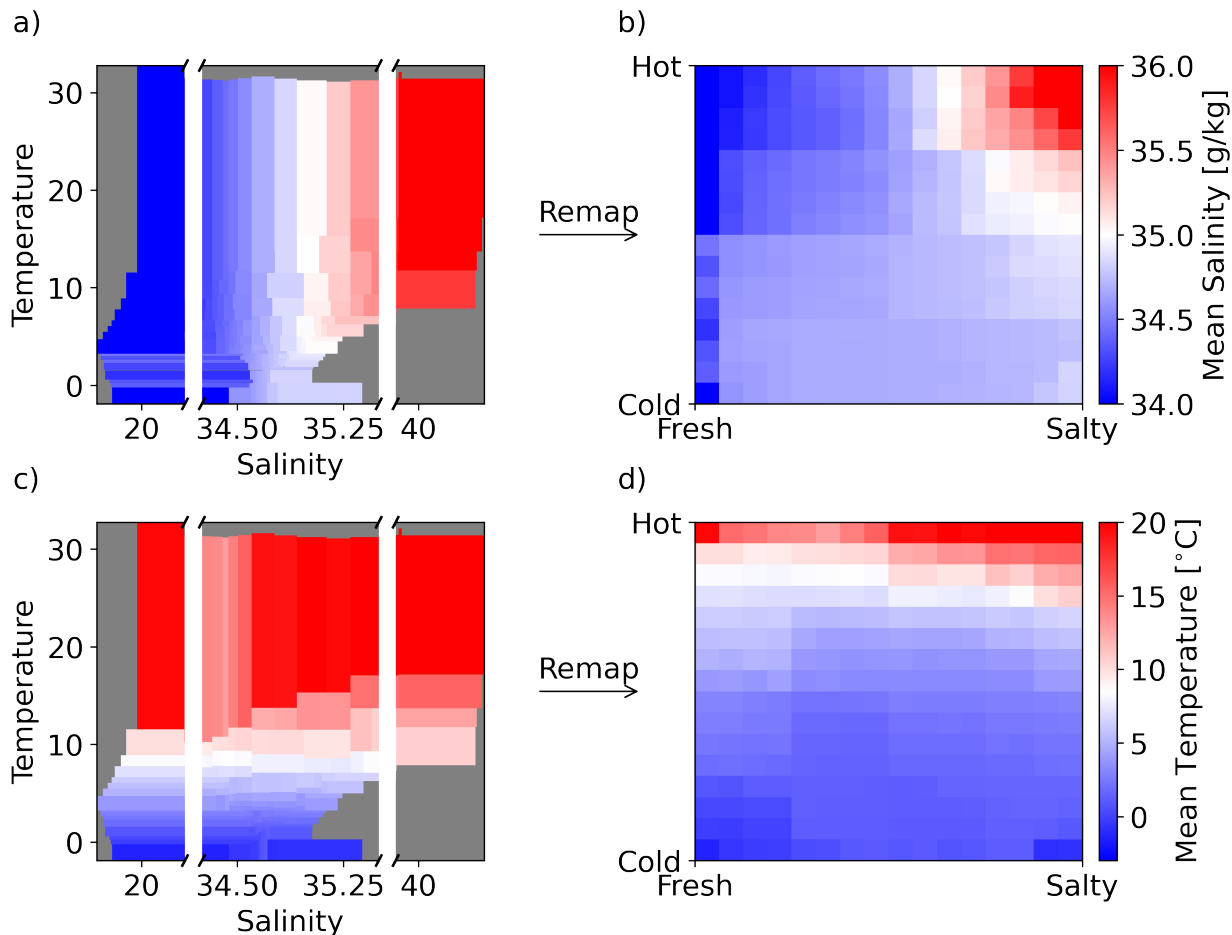


233 FIG. 3. BSP splitting on alternating axes with 2^8 bins, applied to the ACCESS-CM2 piControl (a and c) depth-
 234 integrated volumetric distribution in latitude-longitude co-ordinates, and (b and d) zonally-integrated volumetric
 235 distribution in latitude-depth co-ordinates. BSP bins are coloured by the time-mean (top row) salinity and
 236 (bottom row) temperature in each bin. Empty cells (where there is no BSP bin) are coloured in grey.

224 figure 3c and d). In order to minimise the shifting of BSP bin limits in response to minute grid-cell
 225 volume changes in the deep ocean, we first take the time-mean of the grid cell volumes and then
 226 use this static field, along with the time varying $T - S$ properties of the grid-cells, to define the BSP
 227 bins and the $T - S$ variability within them.

228 The coarse vertical resolution also impacts the results in $T - S$ space, as regions that are strongly
 229 stratified (but coarsely resolved vertically) will have significant gaps in temperature and salinity
 230 when re-projected onto $T - S$ space. The impact of coarse vertical resolution in the model can be
 231 reduced by linearly interpolating the vertical model grid. In section 5, we show how our results
 232 change when the vertical model grid resolution is doubled and quadrupled via linear interpolation.

237 Note that in BSP, the choice of which axis to cut along, or indeed the angle of the line that
 238 makes the cut, is entirely arbitrary. If choosing to cut orthogonal to the distribution axes, there
 239 exist 2^n combinations of the order of subdivision that are valid. More generally, the choice to
 240 slice orthogonally to an axis is also arbitrary, and the BSP algorithm could, for instance, be
 241 directed to modify its angle until the volume constraint $\frac{1}{2^n} \iint v(x, y) dx dy$ is met. However, not all
 242 combinations are physically plausible when subdividing the ocean in $T - S$ or Eulerian space, and



249 FIG. 4. Remapping BSP bins from (a and c) real $T - S$ space, to (b and d) relative $T - S$ space based on a binary
 250 tree structure. BSP bins are coloured by (a and b) time-mean salinity, and (c and d), time-mean temperature in
 251 the ACCESS-CM2 piControl run. Empty cells (where there is no BSP bin) are coloured in grey.

243 we opt to focus hereafter on the specific case of orthogonal slices alternating between the y - and
 244 x - axes ($yxyxyxyx$ for 8 cuts). This order of BSP split combinations preserves the aspect ratio
 245 of BSP bins, ensuring a more equivalent representation of x - and y - variability. We explore this
 246 aspect ratio argument, and impact of choosing to slice along other orders of subdivision, in the
 247 Appendix, and reserve exploration of non-orthogonal slices in BSP for future work.

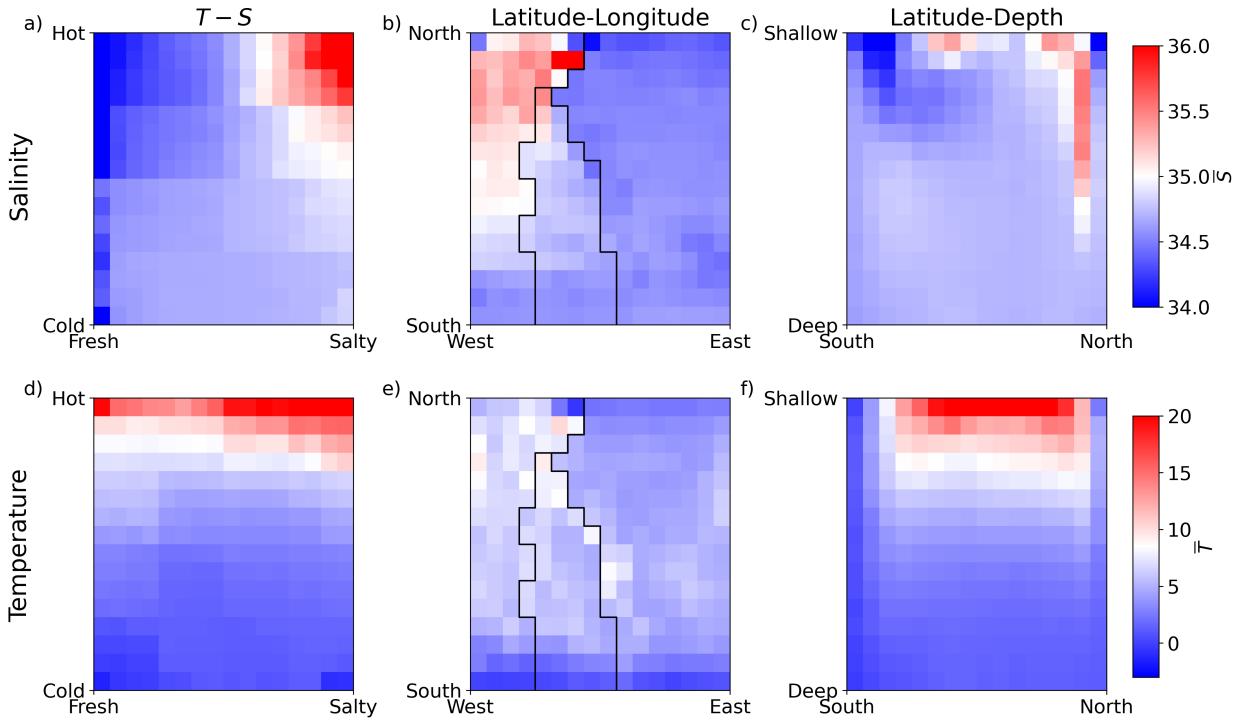
248 *b. Visualising 2D BSP framework*

252 In Eulerian space, the BSP bins generally align with the regular latitude-longitude (and latitude-
 253 depth) grid, as demonstrated by the general uniformity in BSP bin size in figure 3. However, in

254 $T - S$ space, the ocean's volume is concentrated over a relatively narrow range of temperatures
255 and salinities (figures 2). Thus, the equal-volume binning using BSP leads to a large difference
256 in the temperature and salinity ranges spanned by a given bin in $T - S$ space. Surface waters
257 (which occupy a large range of temperatures and salinities but represent minimal volume) are over-
258 represented in the visualisation, as exhibited in figure 4a. Instead, it is advantageous to visualise
259 each bin with an equal area in order to more clearly convey the equal-volume nature of the BSP
260 framework. In order to achieve this, we make use of the binary tree structure obtained from the BSP.
261 By construction, the corner bins obtained from the BSP (i.e, the top-right, top-left, bottom-right
262 and bottom-left bins) represent the extrema in $T - S$ space. All other bins are situated relative to
263 these extrema in the BSP tree, and can be remapped relative to these corner bins. Hence, we remap
264 the bins obtained from BSP onto a plot relative to the ocean's extrema.

265 In figure 4, we plot the output of this remapping in $T - S$ space. We plot the mean salinity (figure
266 4a and b) and the mean temperature (figure 4c and d) within each BSP bin in $T - S$ and in remapped
267 $T - S$ space. The remapping effectively preserves the fresh-to-salty and hot-to-cold gradient of
268 temperature and salinity in each bin (figure 4b and d). The use of the BSP tree structure in the
269 remapping ensures that each bin (representing a single unit of volume) is saltier (fresher) and hotter
270 (colder) than the bin to its left (right) and below (above) it. The fact that we 'tag' each BSP bin in
271 this relative space also means that in time series where the overall volume distribution of the ocean
272 changes (for instance, in the historical run), the BSP bins will remain positioned relative to one
273 another, and thus will stay comparable as the x^{th} percentile warmest (coldest), saltiest (freshest)
274 bin in the model run.

279 The characteristic salinity and temperature of the global ocean can be seen in the remapped
280 BSP plots in all coordinate systems (figure 5). The salty North Atlantic is visible in the top left
281 of figure 5b and right side of figure 5c, while the relatively fresher Pacific and Southern Oceans
282 are evident in the bottom and right hand side of figure 5b and top left of figure 5c, respectively.
283 The clear thermal stratification of the global ocean through depth is also retained in the remapped
284 latitude-depth plots, as shown in figure 5f. Overall, the latitude-depth BSP diagnostic aligns well
285 with traditional zonally-averaged plots (not shown). However, there are some clear differences
286 between the two diagnostics. Low volume regions are naturally collapsed in the BSP framework
287 and combined with other, adjacent water masses to reach the equal-volume constraint. This is



275 FIG. 5. Time-mean (a - c) salinity and (d - f) temperature in remapped equal-volume BSP bins, in (a and d)
 276 $T - S$, (b and e) latitude-longitude, and (c and f) latitude-depth co-ordinates, from the ACCESS-CM2 piControl
 277 simulation. The vertical black lines in panels b and e roughly delineate the Atlantic (left), Indian (center) and
 278 Pacific (right) basins.

288 particularly true for the Arctic, which occupies the northern high latitudes but has a low overall
 289 volume and thus is collapsed to the rightmost BSP bins in figures 5c and f. The (fresh) tropical
 290 and (salty) sub-tropical surface waters are also collapsed to a handful of bins near the surface of
 291 the ocean in figure 5c.

292 In this work, we present all results in the form of this remapped BSP visualisation, as it provides
 293 equal visual weight to each volume of ocean regardless of the space occupied by each bin in
 294 its original coordinate system. This remapping also retains the salient features of the different
 295 coordinate systems while presenting the data on an equivalent constant-volume metric, enabling a
 296 cleaner comparison between different coordinate systems. For ease of interpretation of the BSP
 297 remapping and further results in $T - S$ space, we show the broad geographic distribution of the
 298 warmest (coldest), freshest (saltiest) 25% volume of the ocean in the Appendix (figure B1).

299 *c. Signal-to-Noise Ratio*

300 The signal-to-noise ratio is commonly employed to determine the relative impact of internal
301 variability in the climate system (e.g., Hawkins and Sutton (2012)). Here, we define signal-
302 to-noise ratio (F/N) as the change in temperature (or salinity) in a given bin over the historical
303 period (1850 to 2014), divided by the standard deviation of the temperature (or salinity) over the
304 pre-industrial control period:

$$F/N = \Delta C / \sigma_{control}, \quad (1)$$

305 where C is any generic tracer. The signal (F) is calculated as the linear trend from 1850 to 2014,
306 multiplied by the number of years in the entire period (165 years). In this work, we calculate F/N
307 for the mean T and S in all BSP bins in $T - S$, latitude-longitude, and latitude-depth co-ordinates
308 (section 5).

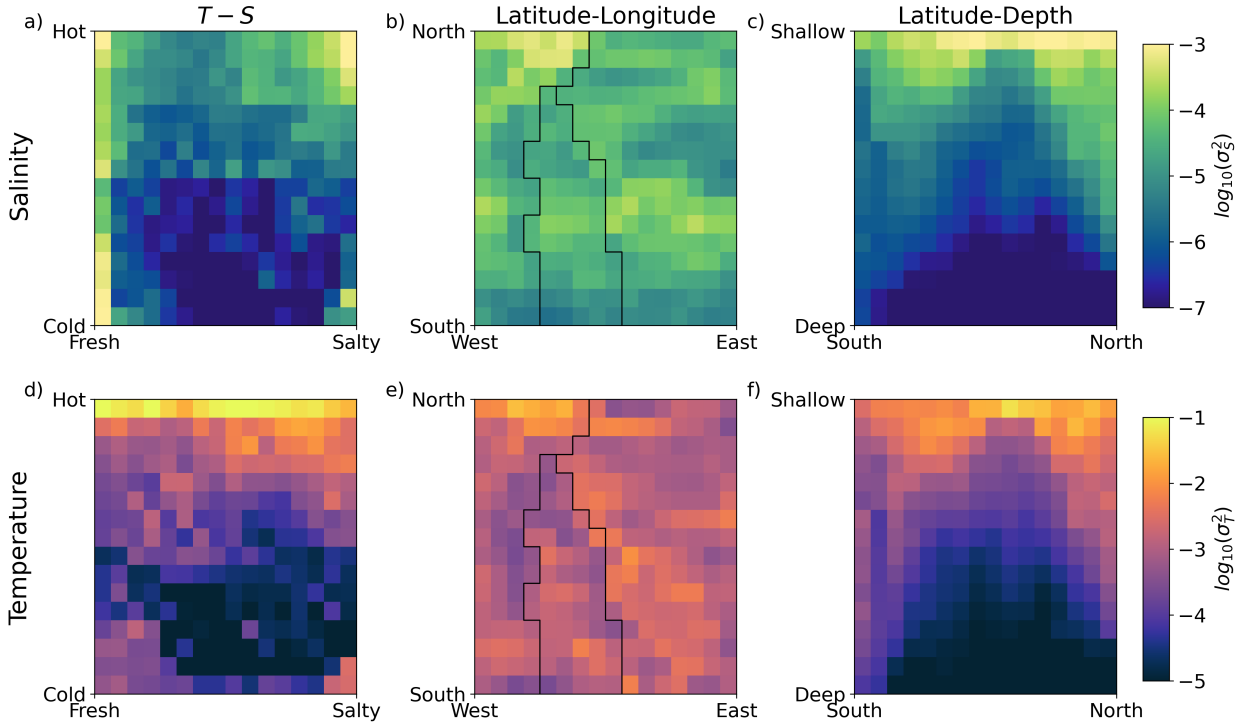
309 **4. Results**

310 The BSP framework enables an equal-volume comparison between three popular two-
311 dimensional coordinate systems used to assess ocean and climatic changes - the temperature-
312 salinity, latitude-longitude, and latitude-depth coordinate systems. In this section, we explore the
313 internal variability, or ‘noise’, in these three co-ordinate systems.

314 *a. Internal Variability*

315 We begin by assessing the internal variability in the mean temperature and salinity of each BSP
316 bin in the three coordinate systems in question. Overall, the $T - S$ coordinate system exhibits
317 a broad range in variance, from low variability in BSP bins corresponding to the ocean interior
318 (bottom-middle bins in figure 6a and d), to high variability in BSP bins corresponding to the
319 ocean’s surface (edge and corner bins in figure 6a and d). The range in variability between surface
320 and interior BSP bins is also reflected in the latitude-depth plots (figure 6c and f), where deep
321 bins have much lower variability than surface bins. Latitude-longitude co-ordinates (which are
322 depth-integrated) tend to have a smaller range in variability overall (figure 6b and e).

323 The difference in variability between different BSP bins, and between co-ordinate systems, can
324 be traced to two possible sources. First, the process of integrating over the ocean volume in

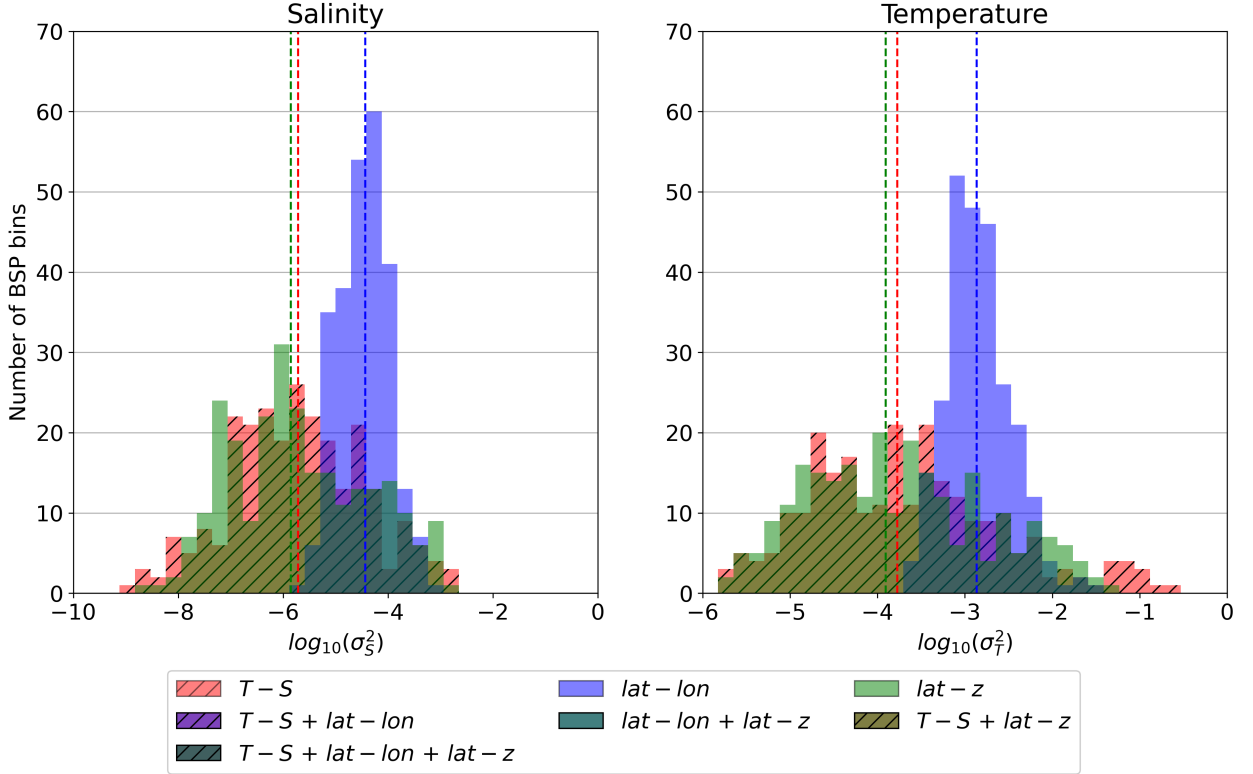


335 FIG. 6. (a - c) Variance in salinity, $\log_{10}(\sigma_S^2)$ and (d - f) temperature, $\log_{10}(\sigma_T^2)$ in equal-volume BSP bins, in
 336 (a and d) $T - S$, (b and e) latitude-longitude, and (c and f) latitude-depth co-ordinates.

325 different co-ordinate systems may lead to differing phase-cancellation characteristics of variability
 326 that varies in space. For example, any modes of variability that result in warming at one longitude
 327 and cooling at another longitude at the same latitude and depth will compensate each other in
 328 that given latitude-depth bin, leading to reduced variability in latitude-depth compared to the
 329 longitude-latitude coordinate where the two phases of the variability are separated.

330 Second, watermass-based co-ordinates exclude by construction adiabatic processes (associated
 331 with, for example, wind-driven circulation changes), which may have a higher amplitude variability.
 332 Thus, the difference between variability in $T - S$ space and its Eulerian counterparts may be due
 333 to the fact that variability in $T - S$ space is due to diabatic processes, while variability in Eulerian
 334 co-ordinates may be due to *both* diabatic and adiabatic processes.

337 The histogram of salinity and temperature variance in each co-ordinate system (figure 7) provides
 338 further insight into differences between watermass-based and Eulerian co-ordinate systems. $T - S$
 339 co-ordinates and latitude-depth co-ordinates have similar median variability, likely for different
 340 reasons - $T - S$ co-ordinates filter out adiabatic processes, resulting in a lower median variability,



350 FIG. 7. Distribution of a) salinity variance, $\log_{10}(\sigma_S^2)$ and b) temperature variance, $\log_{10}(\sigma_T^2)$ across all BSP
 351 bins in $T - S$ (red), latitude-longitude (blue) and latitude-depth (green) co-ordinates. Dashed lines show the
 352 median variance for each co-ordinate system.

341 while latitude-depth co-ordinates naturally highlight deep ocean processes separate from the surface
 342 ocean, leading to a lower median variance. Latitude-longitude co-ordinates, on the other hand,
 343 have a higher median variance.

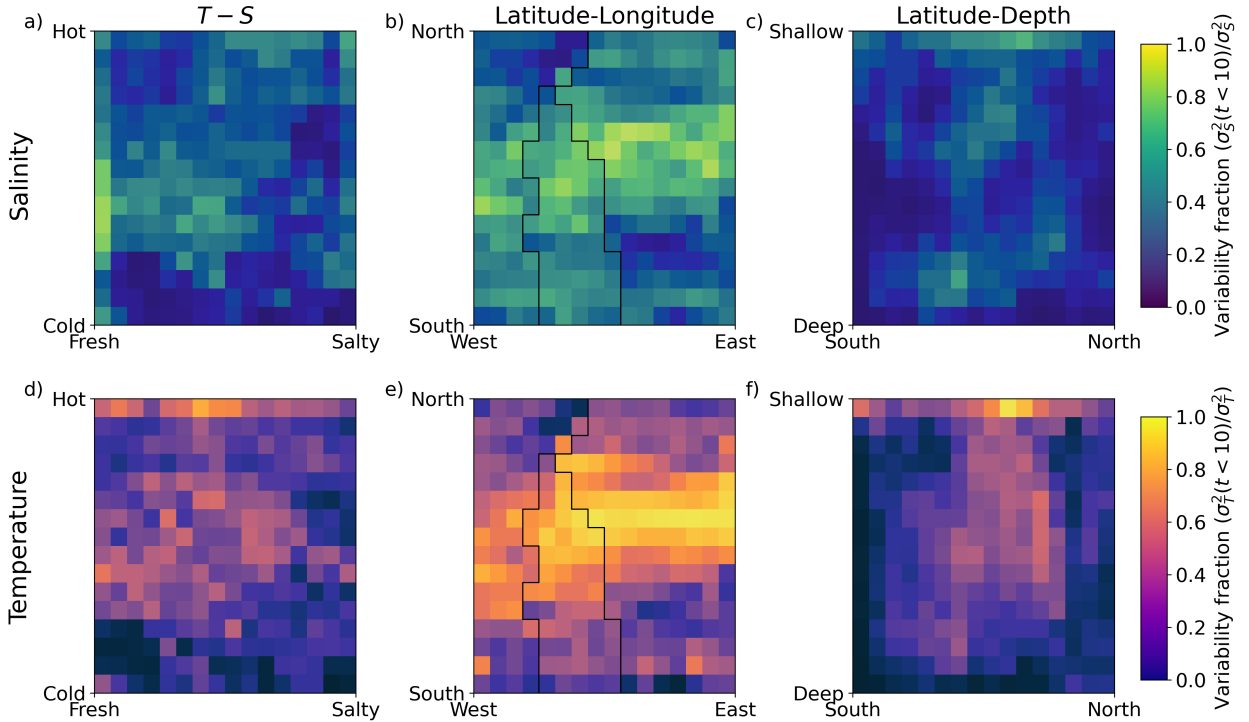
344 In order to assess how statistically different these histograms are, we apply the Kolmogorov-
 345 Smirnov (K-S) test of ‘goodness of fit’ between histogram pairs. The K-S test assesses the
 346 probability that a given pair of distributions were randomly sampled from the same data. The $T - S$
 347 and latitude-depth histograms are identified as the only statistically similar pair of histograms,
 348 implying that the medians (red and green lines) may not be statistically different. No other
 349 distributions in this analysis pass the K-S test for statistical similarity.

353 As discussed in section 1, moving from one-dimensional temperature co-ordinates to two-
 354 dimensional $T - S$ co-ordinates can enable a cleaner separation of surface and ocean interior
 355 watermasses due to the addition of the salinity co-ordinate. The histograms in figure 7 indicate

356 that this separation leads to a more skewed distribution of variance, with a large number of weakly
357 varying interior bins and a small handful of surface ocean bins (note the logarithmic x-axis). Due
358 to this skewness, the mean variance across the entire distribution (as calculated in the 1D case in
359 Holmes et al. (2022)) for our 2D case is strongly impacted by surface bins (which have higher
360 variance). On the other hand, the median variance (vertical lines in Fig. 7) is lower, reflecting the
361 much more numerous interior BSP bins. Moving forward, we opt to compare the median terms of
362 interest, though we do explore the difference between mean and median variance in our spectral
363 analysis below.

364 The internal variability in figure 6 is a consequence of inter-annual and sub-decadal ocean pro-
365 cesses, (<10 year periods, such as the El-Niño Southern Oscillation and North Atlantic Oscillation),
366 and multi-decadal and centennial processes (>10 year periods, such as Atlantic Meridional Over-
367 turning Circulation variability). In order to parse the relative influence of sub-decadal processes
368 on internal variability, we present the variability of the 10-year high-pass filtered temperature and
369 salinity signal relative to the total temperature and salinity variability, in figure 8. A fraction of
370 1 in figure 8 indicates that all of the variability in the given bin may be attributed to sub-decadal
371 processes, while a fraction of 0 indicates that all of the variability in the given bin may be attributed
372 to multi-decadal processes. Overall, variability in latitude-depth coordinates is influenced most by
373 multi-decadal processes (figure 8c and f), likely due to the emphasis on deep ocean processes which
374 change minimally over time in this co-ordinate system. The bulk of variability in $T - S$ co-ordinates
375 is also due to multi-decadal processes. Surface waters in $T - S$ and latitude-depth space (edge bins
376 in figure 8a, c, d and f) have a high proportion of sub-decadal variability. Latitude-longitude
377 co-ordinates have a higher fraction of sub-decadal variability overall, particularly in the North
378 Atlantic and Equatorial Pacific (possibly due to the influence of ENSO; figure 8b and e).

382 The difference between different co-ordinate systems is highlighted by plotting the distribution of
383 proportion of sub-decadal variance (see figure 9). In latitude-depth space, approximately 80–85%
384 of the total variability comes from > 10 year processes (green dashed lines in figure 9), again due
385 to the over-representation of deep ocean volumes in this co-ordinate system. $T - S$ co-ordinates
386 also host a high proportion of multi-decadal processes, with the overall multi-decadal variability
387 representing 77–80% of the total, suggesting that diabatic processes tend to occur, on average,
388 at multi-decadal timescales (red dashed lines in figure 9). In contrast, around 50% of the total

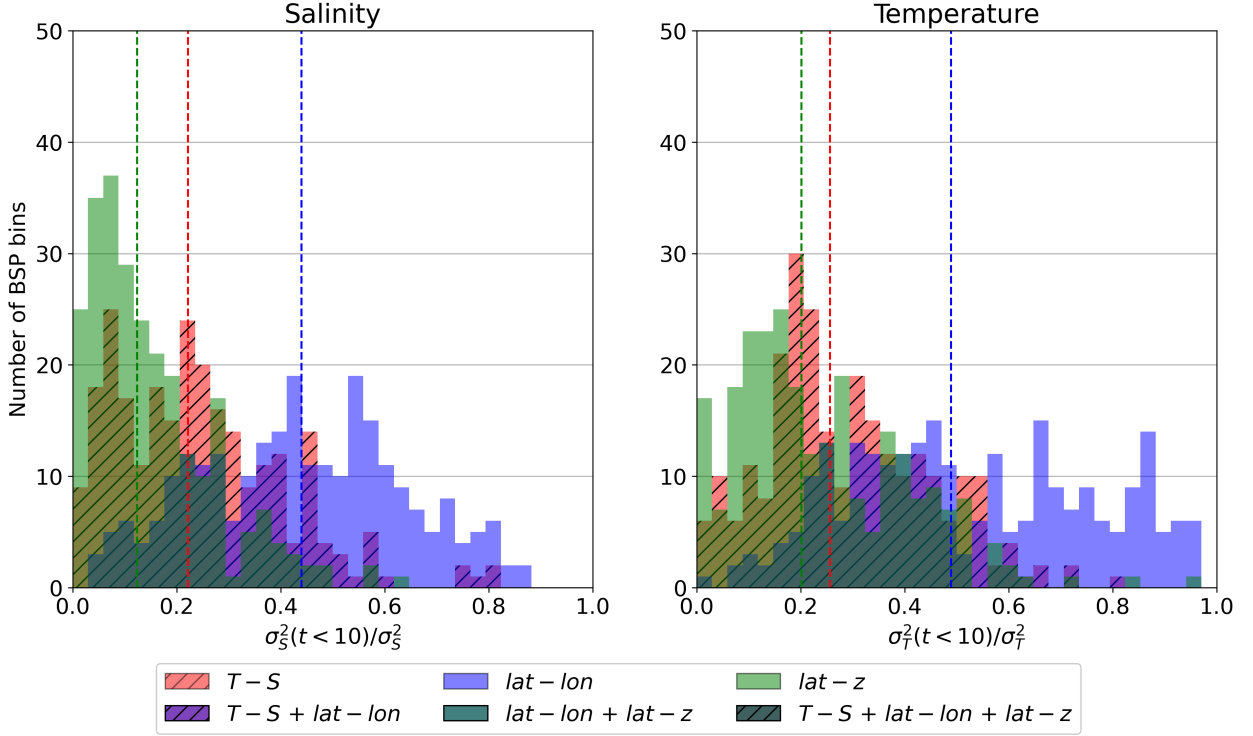


379 FIG. 8. Proportion of variance due to sub-decadal processes, (a - c) in salinity $\sigma_S^2(t < 10)/\sigma_S^2$ and (d - f)
 380 in temperature $\sigma_T^2(t < 10)/\sigma_T^2$, in (a and d) $T - S$, (b and e) latitude-longitude, and (c and f) latitude-depth
 381 co-ordinates.

388 salinity and temperature variability in latitude-longitude space comes from > 10 year processes
 389 (blue dashed lines in figure 9). These results are consistent with the one-dimensional analysis of
 390 Holmes et al. (2022) who showed that the mean temperature variance in a 1D temperature-based
 391 coordinate became comparable to variability in one-dimensional depth and latitude co-ordinates at
 392 decadal to multi-decadal time-scales, where diabatic processes dominate.
 393

397 The variability fractions presented here are stable across all feasible BSP split combinations
 398 (figure A1). For all split combinations, a lower fraction of variability comes from sub-decadal
 399 processes in latitude-depth and $T - S$ co-ordinates compared with latitude-longitude co-ordinates.

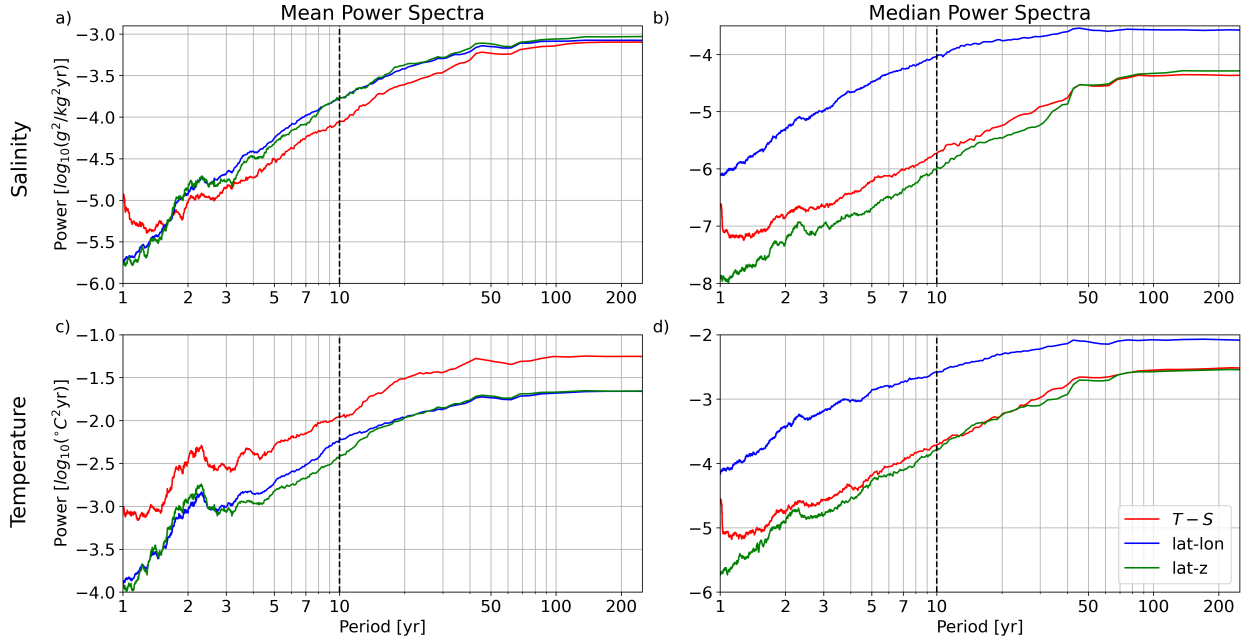
405 The variability in all three co-ordinate systems may be further broken down into characteristic
 406 timescales using spectral analysis, as shown in figure 10. As highlighted earlier, mean variance
 407 is more sensitive to outlier values in the skewed distributions presented. As a consequence, mean
 408 power spectra (figure 10a and c) are more impacted by outlier (often surface) sources of variability.
 409 Our mean results in figure 10c compare with the prior one-dimensional analysis of Holmes et al.



394 FIG. 9. Distribution of proportion of variance due to sub-decadal processes a) in salinity $\sigma_S^2(t < 10)/\sigma_S^2$ and
 395 b) in temperature $\sigma_T^2(t < 10)/\sigma_T^2$ across all BSP bins in $T-S$ (red), latitude-longitude (blue) and latitude-depth
 396 (green) co-ordinates. Dashed lines show the median variance proportion for each co-ordinate system.

410 (2022) (specifically, figure 11a in Holmes et al. (2022)). The mean power spectra of temperature
 411 shows a clear peak in the 2 - 3 year time period in temperature in all coordinate systems (figure
 412 10c), aligning with findings by Holmes et al. (2022), who concluded that this peak is likely due to
 413 ENSO. Holmes et al. (2022) found that the mean temperature variability in T space exceeds that in
 414 depth space at $t > 10$ years.

415 The median power spectra, that is, the median of all power spectra at each timescale, is a means
 416 of comparison between co-ordinate systems which is more reflective of the more numerous ocean
 417 interior bins. The median power spectra highlight the similarity between latitude-depth and $T-S$
 418 co-ordinates (figures 10b and d). Across all time periods, median variance in $T-S$ space is similar
 419 (but slightly higher) than that in latitude-depth space. Overall, latitude-longitude co-ordinates have
 420 the highest median variance across most time periods.

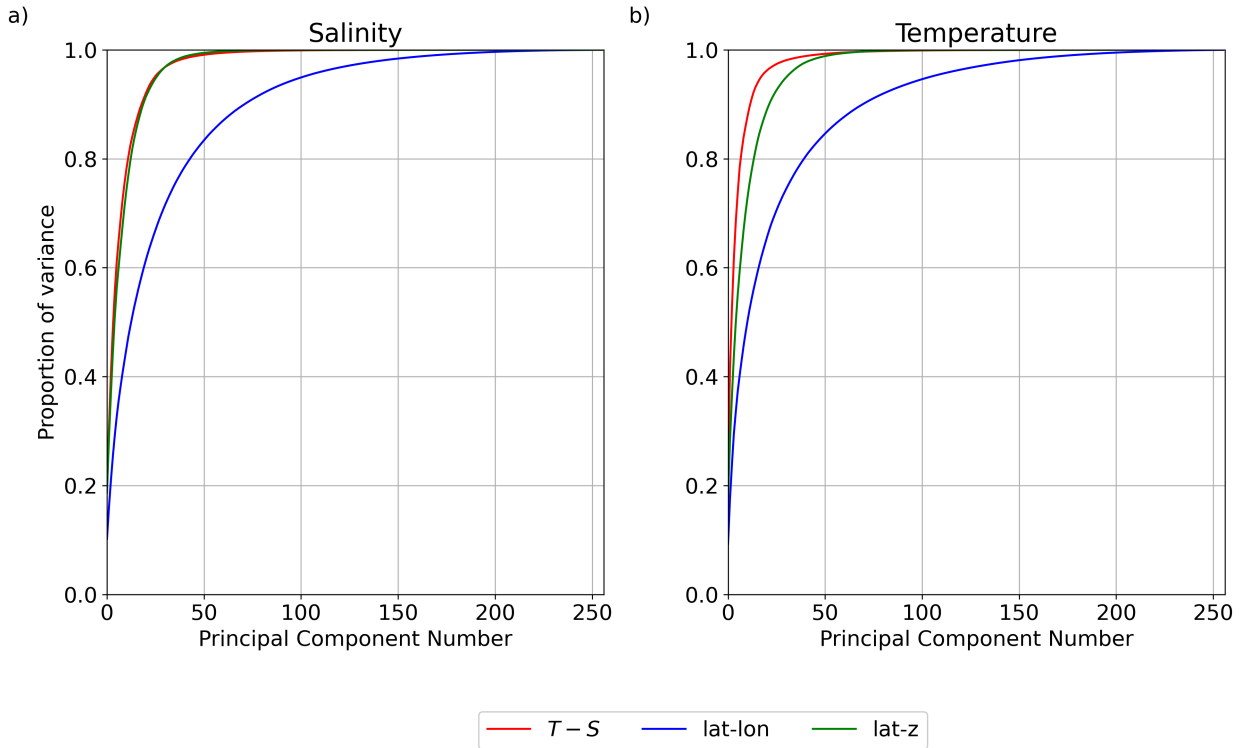


400 FIG. 10. Power spectra of (a and b) salinity variability and (c and d) temperature variability in $T-S$ co-ordinates
 401 (red), latitude-longitude co-ordinates (blue) and latitude-depth co-ordinates (green). Spectra are presented both
 402 as the mean of all BSP bins (a and c) and the median of all BSP bins (b and d). The vertical dashed line shows a
 403 period of 10 years, the cutoff used in figure 8. Power spectra are calculated from monthly data, using Thompson’s
 404 multitaper method with 19 Slepian tapers.

421 *b. Modes of Variability*

422 The primary modes of variability that drive internal variability in the three coordinate systems
 423 may be explored via Principal Component Analysis (PCA), where a principal component (PC) is
 424 the eigenvector of the covariance matrix of the distribution. The correlation coefficients obtained
 425 from PCA can indicate dominant modes of variability in the time series. PCA yields several PCs
 426 which collectively explain the total variance in a time series. We can thus find the number of PCs
 427 needed to adequately explain a high proportion of variance in a time series – the lower the number
 428 of PCs, the ‘simpler’ the time series can be considered to be. Figure 11 shows the cumulative
 429 proportion of variance explained by the PCs obtained from PCA.

430 $T-S$ and latitude-depth co-ordinates capture total salinity variance with the fewest PCs, while
 431 $T-S$ co-ordinates are superior in capturing temperature variance with the fewest PCs (compare
 432 green and red lines in figure PCAs). In $T-S$ space, 95% of the total temperature variance is



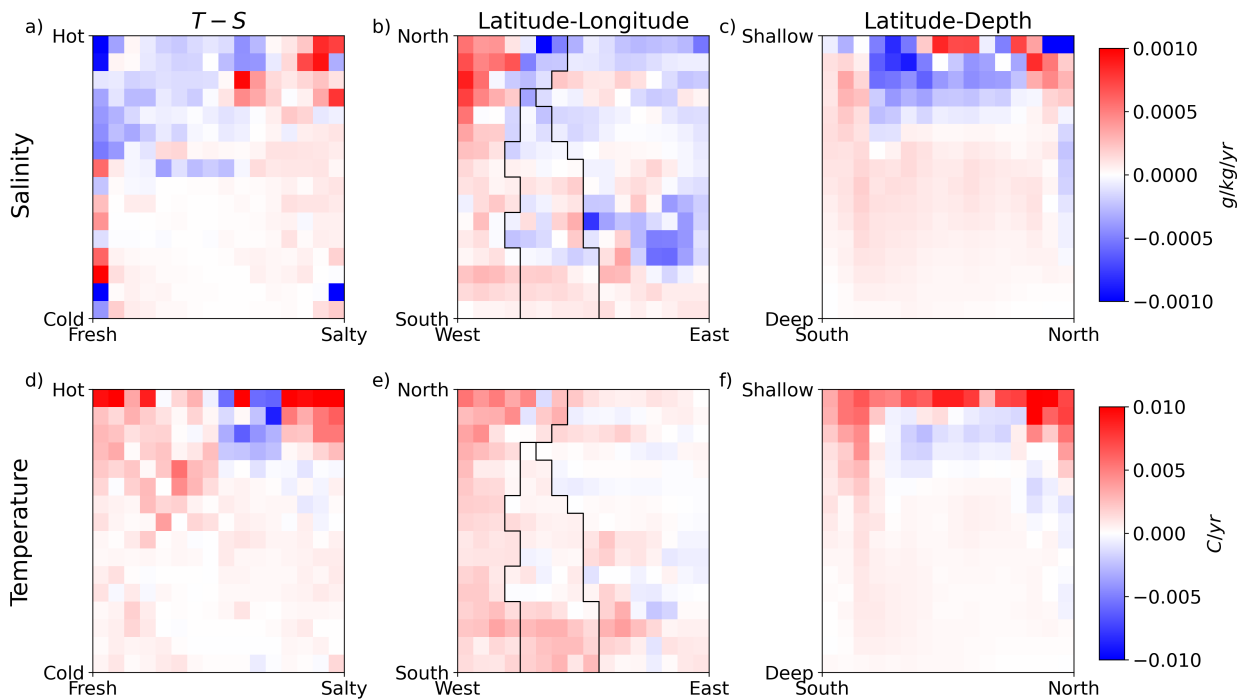
435 FIG. 11. Cumulative proportion of total variance captured by principal components in the Principal Component
 436 Analysis, for monthly a) salinity, and b) temperature, in $T-S$ co-ordinates (red), latitude-longitude co-ordinates
 437 (blue) and latitude-depth co-ordinates (green).

433 captured in 17 principal components, while in latitude-depth and latitude-longitude co-ordinates
 434 31 and 104 PCs respectively are required to capture 95% of temperature variance.

438 In the salinity time series (figure 11b), 95% of variance can be captured by 26, 25, and 101
 439 PCs in $T-S$ space, latitude-depth space and latitude-longitude space, respectively. Thus, while
 440 $T-S$ co-ordinates remain the preferred choice to express temperature variability most simply,
 441 latitude-depth presents an equivalent alternative for salinity variability.

442 5. Discussion: Implications for signal-to-noise ratio

443 Overall, our results so far show that the projection of internal variability, or ‘noise’ in the
 444 global ocean, into latitude-depth and $T-S$ co-ordinates is roughly equivalent, and is lower than
 445 latitude-longitude co-ordinates. Here we assess the ‘signal’, that is, the historical temperature and
 446 salinity tendency, in $T-S$, latitude-depth space and latitude-longitude space. Figure 12 shows the



457 FIG. 12. Linear trend in historical (a - c) salinity (in $g/kg/year$) and (d - f) temperature (in $^{\circ}C/year$), in (a and d)
 458 $T - S$, (b and e) latitude-longitude, and (c and f) latitude-depth co-ordinates, from 1970-2014. The linear trend
 459 is calculated by finding the slope of the linear regression on monthly data from January 1970 to December 2014.

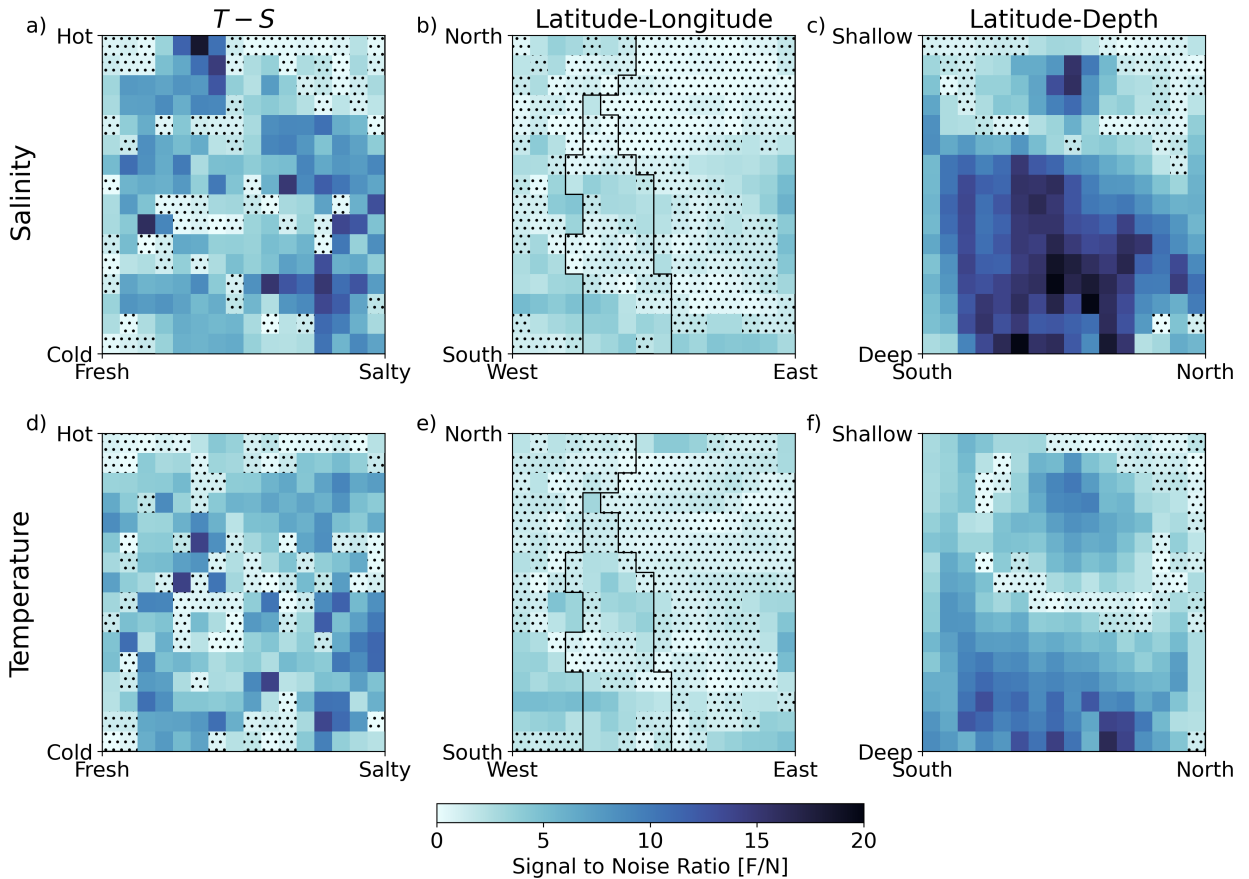
447 temperature and salinity tendencies from 1970 to 2014 in the ACCESS-CM2 historical simulation.
 448 The salinity tendency (figure 12a, b and c) aligns with previous model and historical estimates
 449 of salt content change. In $T - S$ space, salty regions get saltier, and fresh regions get fresher,
 450 following a ‘wet-gets-wetter-dry-gets-drier’ pattern (Allan et al. 2020). This is most pronounced in
 451 the warmest 50% of the ocean in $T - S$ space, corresponding with the surface ocean that experiences
 452 widening salinity contrasts first. The Antarctic Intermediate Water is freshening and sub-tropical
 453 waters are becoming more saline, aligning well with observations of salinity change (see figure
 454 12c). Tropical salinity changes are not as obvious in this framework as the tropics constitute a
 455 relatively small proportion of the global ocean volume. Overall, the changes in salinity in $T - S$
 456 space and latitude-depth space align with findings by Sohail et al. (2022); Silvy et al. (2020).

460 Temperature tendency in a fixed-volume framework is proportional to heat content change, so
 461 the temperature tendencies presented in figure 12d, e and f may be thought of as equivalent to the
 462 ocean heat content change. In $T - S$ space, there is broad warming over almost all water masses

463 in the 50% warmest BSP bins, save a small water mass in a warm, salty quadrant of the global
464 ocean. Further exploration (not shown) suggested this cooling patch may have originated in the
465 tropical and sub-tropical Pacific, though the watermasses corresponding to the cooling also exist
466 in the Indian and Atlantic sectors. This warming profile is consistent, at least in temperature space
467 and depth space, with findings by Sohail et al. (2021). Thus, the BSP remapping captures well
468 previously observed trends in ocean heat and salt content, lending credence to the method as a
469 means to assess changes in historical temperature and salinity, or the climate change ‘signal’.

470 Having quantified both the temperature and salinity signal and noise in the climate system, we
471 proceed to test the signal-to-noise ratio across the three co-ordinate systems of interest. We focus
472 on the entire historical signal, from 1850 to 2014, as our climate ‘signal’ (note that this is in contrast
473 to other detection and attribution studies which look at the recent past since 1950, e.g. Pierce et al.
474 (2012)). We follow equation (1) to calculate signal-to-noise ratio, and use the linear trend over
475 the historical period (i.e., C in 2014 minus C in 1850), multiplied by the number of years (165)
476 as ΔC in the signal-to-noise ratio calculation. The signal-to-noise ratio in $T - S$, latitude-depth
477 and latitude-longitude space is shown for each BSP bin in figure 13, for salinity (panels a-c), and
478 temperature (panels d-f).

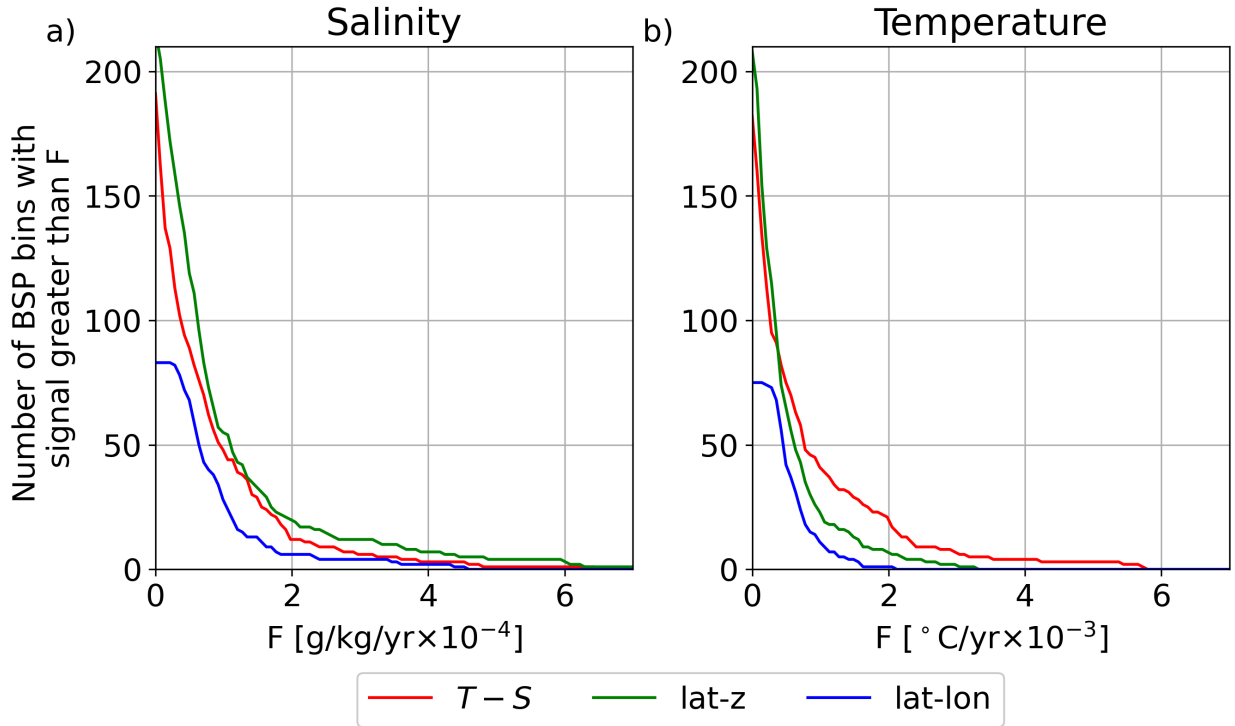
482 Latitude-depth co-ordinates broadly show the highest signal-to-noise ratio, with a
483 large proportion of bins having a signal which exceeds twice the standard deviation of the pre-
484 industrial control simulations $F/N > 2$, particularly in the deep ocean. Latitude-depth F/N is
485 especially high for salinity (figure 13c), particularly in the deep ocean. This is in contrast to
486 previous studies that have found the anthropogenic signal to be most pronounced in the surface
487 ocean relative to noise (e.g. Pierce et al. (2012)). This is likely because we choose to assess our
488 signal, F , as the linear trend over the entire historical period (1850-2014), rather than the recent
489 past since 1950 considered by other detection and attribution studies. Thus, the long-term changes
490 to deep ocean salinity and temperature are more readily picked up, and at the same time surface
491 temperature and salinity changes are lower in a relative sense. Given the sharp contrast in variance
492 between the surface and deep bins, this leads to a relatively large F/N in the deep ocean compared
493 to the surface. Our analysis also shows a high temperature F/N in water masses corresponding
494 to Subantarctic Mode Waters (figure 13f), consistent with past research (Banks et al. 2000, 2002;
495 Swart et al. 2018; Hobbs et al. 2021).



479 FIG. 13. Signal-to-noise ratio of (a - c) salinity and (d - f) temperature, in (a and d) $T - S$, (b and e) latitude-
 480 longitude, and (c and f) latitude-depth co-ordinates. Stippling shows BSP bins with a signal-to-noise ratio,
 481 $F/N < 2$.

496 $T - S$ coordinates also perform relatively well in isolating the forced signal, with the hot-spots of
 497 F/N broadly distributed across the $T - S$ co-ordinates in both salinity and temperature. Latitude-
 498 longitude coordinates perform the worst in isolating the historical forced signal from internal
 499 variability, with the majority of bins having a relatively low signal-to-noise ratio, in both salinity
 500 and temperature.

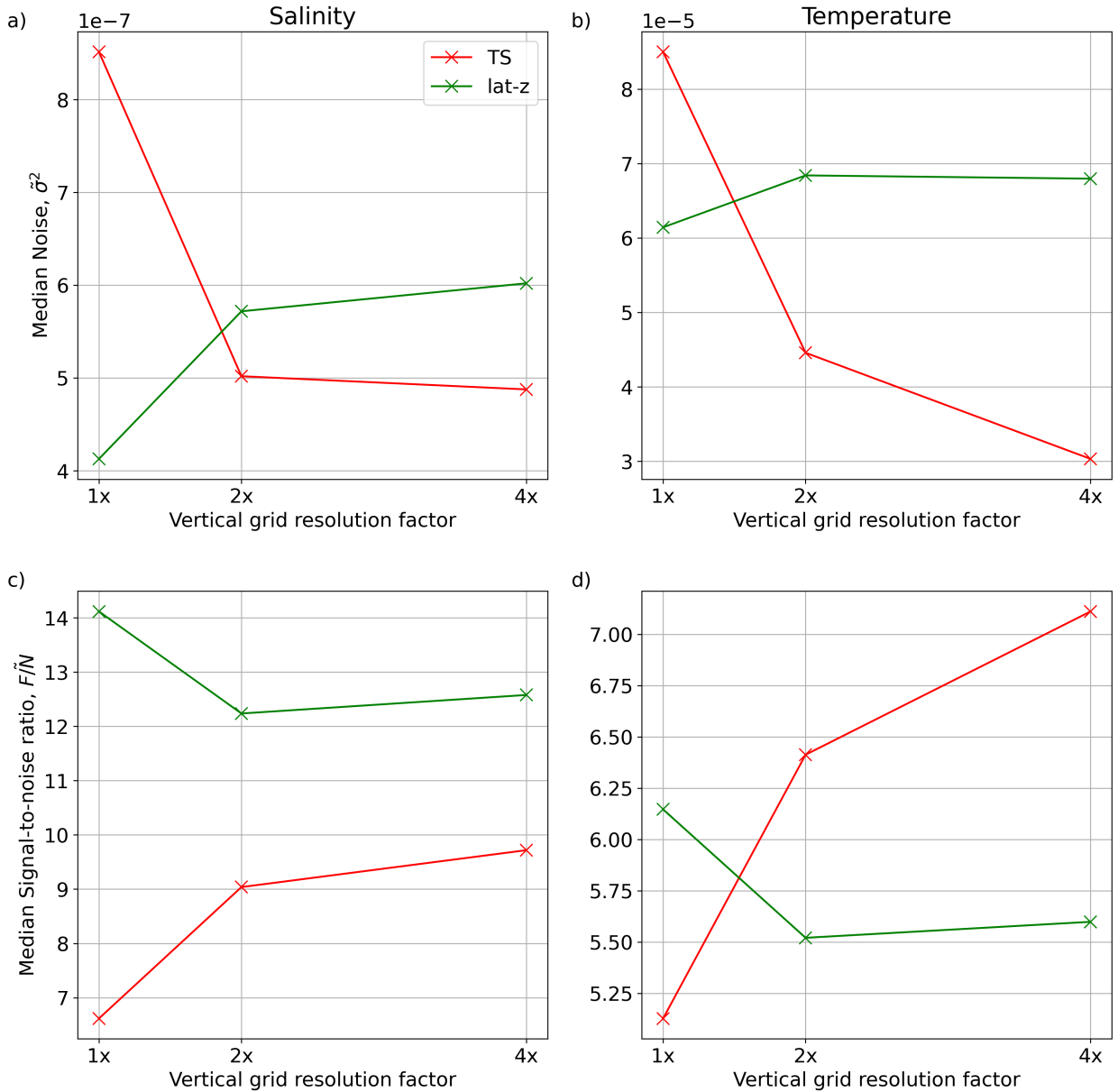
504 While latitude-depth co-ordinates clearly show the greatest F/N across the different co-ordinate
 505 systems assessed here, these bins appear to be isolated to the deep ocean, which does not exhibit
 506 a particularly strong climate change signal (as shown in figure 12c and f). A co-ordinate system
 507 which has enhanced F/N in regions of high T and S change is of particular utility, as these are
 508 the regions of most interest for future studies. In order to investigate this, we plot the cumulative



501 FIG. 14. Number of BSP bins with signal greater than F for each co-ordinate system, $T - S$ (red), latitude-
 502 longitude (blue) and latitude-depth (green), in (a) salinity and (b) temperature. Only bins with a signal-to-noise
 503 ratio of $F/N > 2$ are accumulated.

509 number of bins with a signal greater than F and an $F/N > 2$ in each co-ordinate system in figure 14.
 510 For salinity (figure 14a), latitude-depth co-ordinates clearly have more BSP bins with $F/N > 2$ across
 511 all signal strengths (but particularly in the high F regime). However, $T - S$ co-ordinates prove to be
 512 superior in isolating high F/N in high temperature change regions. While latitude-depth overall
 513 has more BSP bins across all signal strengths for temperature, this advantage is isolated to lower
 514 signal regions, and thus may not be as useful. Hence, $T - S$ co-ordinates are superior to their
 515 Eulerian counterparts in capturing the climate change signal in temperature, due to a high F/N in
 516 regions of high temperature change, F .

521 The results and discussion have so far focussed on analysis of the native ACCESS-CM2 model
 522 grid. However, as flagged in section 3, increasing the vertical resolution of the model grid may
 523 change the representation of variability in $T - S$ and latitude-depth space, altering the conclusions
 524 of this study. In figure 15, we show how the median noise and signal-to-noise ratio in $T - S$



517 FIG. 15. The median (a and b) noise and (c and d) signal-to-noise ratio of (a and c) salinity and (b and d)
 518 temperature, given a doubling (2x) and quadrupling (4x) of the native model vertical grid via linear interpolation.
 519 The first 100 years of the ACCESS-CM2 control simulation are analysed here. Only $T - S$ (red) and latitude-depth
 520 (green) co-ordinates are compared.

525 and latitude-depth co-ordinates changes with a doubling and quadrupling of the model vertical
 526 resolution. As vertical resolution increases, the median noise in $T - S$ space decreases for both
 527 temperature and salinity (figure 15a and b). In latitude-depth space, the median variance increases,

528 though not by as much as variance decreases in $T - S$ space, implying that $T - S$ co-ordinates are
529 more sensitive to vertical model resolution. Therefore, models with a native Eulerian grid will
530 naturally be better represented in Eulerian co-ordinate systems, but as the vertical grid resolution
531 increases, the representation of T and S is improved, enhancing the utility of $T - S$ co-ordinates as
532 a diagnostic tool.

533 The gap in median signal-to-noise ratio between latitude-depth and $T - S$ narrows for salinity
534 as vertical resolution increases (figure 15c). For temperature, the median signal-to-noise ratio
535 in $T - S$ becomes larger than that in latitude-depth upon doubling of the vertical grid resolution
536 (figure 15c). Hence, it is essential to use a model which adequately resolves vertical structures of
537 temperature and salinity to unlock the key benefits of water mass co-ordinates. The F/N in regions
538 of high T and S change (as shown in figure 14) does not change significantly with different vertical
539 resolutions (not shown). Therefore, one of the the main conclusions of this study, that is, that
540 watermass co-ordinates isolate the historical temperature change signal, is robust regardless of the
541 model vertical resolution.

542 There are several questions open for further exploration, particularly in terms of the BSP algorithm
543 presented here. In the past, watermass-based frameworks have been used to develop simple ocean
544 heat and salt content budgets, wherein salt and heat content tendencies can be related solely to
545 diabatic air-sea flux and mixing processes (Holmes et al. 2019; Sohail et al. 2021; Bladwell et al.
546 2021). In the two-dimensional BSP framework, such a budget is more difficult to formulate, as
547 changes to the properties of a bin can potentially change the BSP bins in adjacent $T - S$ regions.
548 That said, the formulation of a budget in the BSP framework would yield a more process-based
549 understanding of some of the trends and variability seen in this analysis, and is reserved for future
550 work. In addition, while the two-dimensional frameworks assessed here retain regional information,
551 the diagnostics are calculated over the entire global data set. An analysis which is confined only
552 to certain regions may provide further guidance towards the driving processes in different regions
553 of the ocean. Such a process-based, regional approach may also aid in understanding the tendency
554 results in figure 12, including the cooling patch in $T - S$ space. In addition, one-dimensional
555 analyses in temperature space have highlighted the potential benefits of using watermass-based
556 co-ordinates to reduce sampling bias arising from adiabatic heave in observations (Palmer et al.
557 2007; Palmer and Haines 2009). BSP presents an opportunity to extract synthetic profiles from

558 climate model data, following Allison et al. (2019), and assess the influence of two-dimensional
559 co-ordinate systems on observational sampling biases and observed heat and salt content.

560 **6. Conclusions**

561 Watermass-based frameworks are becoming popular for capturing changes in ocean heat and
562 salt content, in part because they are believed to reduce internal variability, thus more effectively
563 isolating the historical ‘signal’ of climate change. However, a rigorous comparison between
564 watermass-based frameworks and Eulerian (latitude-longitude, latitude-depth, etc.) co-ordinate
565 systems has been difficult due to fundamental differences in the way these co-ordinate systems
566 are formulated. In this work, we introduce a statistical method, called *Binary Space Partitioning*
567 (BSP) to recast $T - S$, latitude-longitude and latitude-depth co-ordinate systems onto an equivalent,
568 equal-volume co-ordinate. Applied to pre-industrial control and historical simulations of a state-
569 of-the-art climate model, ACCESS-CM2, BSP enables an apples-to-apples comparison of internal
570 variability between watermass-based and Eulerian co-ordinates. We find that $T - S$ and latitude-
571 depth co-ordinates have equally low global variability, and the majority of this variability can
572 be attributed to multi-decadal processes in both co-ordinate systems. Overall, we find that the
573 historical temperature signal is more effectively isolated in $T - S$ space, with a signal-to-noise ratio
574 that is greater than its Eulerian counterparts in regions of high temperature change. Latitude-depth
575 co-ordinates, on the other hand, present the best option for isolating the historical salinity change
576 signal, with a signal-to-noise ratio that is greater than $T - S$ and latitude-longitude co-ordinates
577 in regions of high salinity change. These results present the lower bound of variance and signal-
578 to-noise ratio in $T - S$ co-ordinates, and are dependent on the model’s vertical grid resolution.
579 Our findings provide a road-map for choosing the best two-dimensional co-ordinate system when
580 analysing global data sets, suggesting that $T - S$ co-ordinates are most appropriate for temperature
581 change studies, and latitude-depth co-ordinates are preferred for salinity change analyses.

582 *Acknowledgments.* We acknowledge the World Climate Research Programme (WCRP), the
583 CMIP6 climate modeling groups for producing and making available their model output, and
584 the Earth System Grid Federation (ESGF) as well as the funding agencies which support the
585 WCRP, CMIP6 and ESGF. All data analysis was conducted at facilities which form part of the Na-
586 tional Computational Infrastructure (NCI), which is supported by the Commonwealth of Australia.

587 The authors are supported by the Australian Research Council (ARC) Centre of Excellence for
588 Climate Extremes (CLEX), the Australian Centre for Excellence in Antarctic Science (ACEAS),
589 and the ARC Discovery Project scheme DP190101173. We acknowledge support from ARC award
590 DE21010004. We thank Dr. John A. Church for assistance in the interpretation of results, and the
591 Climate Modelling Support (CMS) team at CLEX for assistance in developing the BSP binning
592 algorithm. We thank reviewers Yona Silvy and Jonas Nycander for their thorough comments and
593 feedback.

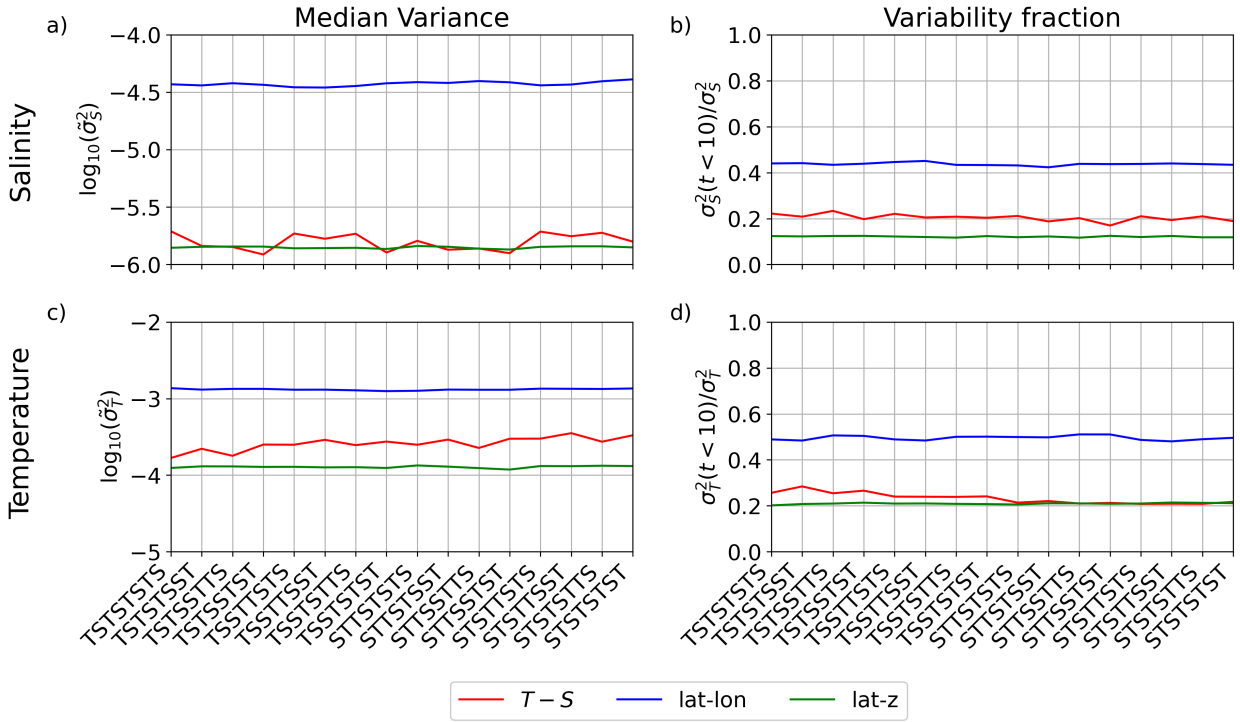
594 *Data availability statement.* All data used in this work is publicly available via ESGF: [https://esgf-](https://esgf-node.llnl.gov/search/cmip6/)
595 [node.llnl.gov/search/cmip6/](https://esgf-node.llnl.gov/search/cmip6/).

596 APPENDIX A

597 **Variability across 2^n combinations of axis subdivisions**

598 In this study, we opt to subdivide alternating axes (starting with the y -axis) 8 times, to yield
599 $2^8 = 256$ bins. However, as mentioned in section 3, there are 256 possible combinations of
600 axis subdivisions that may have been chosen, including $xxxxxxx$, $xxxxxxy$, $yyyyyyx$, etc. In
601 this appendix, we explore the influence of choosing some of these other combinations of axis
602 subdivisions on our results.

603 When assessing internal variability in two-dimensional tracer space, an ideal coordinate system
604 would equally represent changes in both the x - and y -axes. For instance, in some climate model
605 grids latitude and longitude have roughly equivalent resolutions as variability in the latitudinal
606 and longitudinal directions is roughly similar. Of course, for the sake of reducing computational
607 complexity, dimensions which are known apriori to exhibit characteristically lower variability may
608 have reduced resolution - for instance, ocean model grids typically have lower depth resolution
609 than latitude or longitude. Without such apriori knowledge of variability in a given dimension, and
610 in an attempt to create a like-for-like co-ordinate system, we argue that the most appropriate BSP
611 split combinations would be ones that preserve the aspect ratio of bins. Thus, we propose that the
612 most physically plausible BSP split combinations are combinations of xy and yx . Always splitting
613 in axis pairs ensures that no long, thin bins are created which span a large range in one dimension
614 but a small range in another dimension.



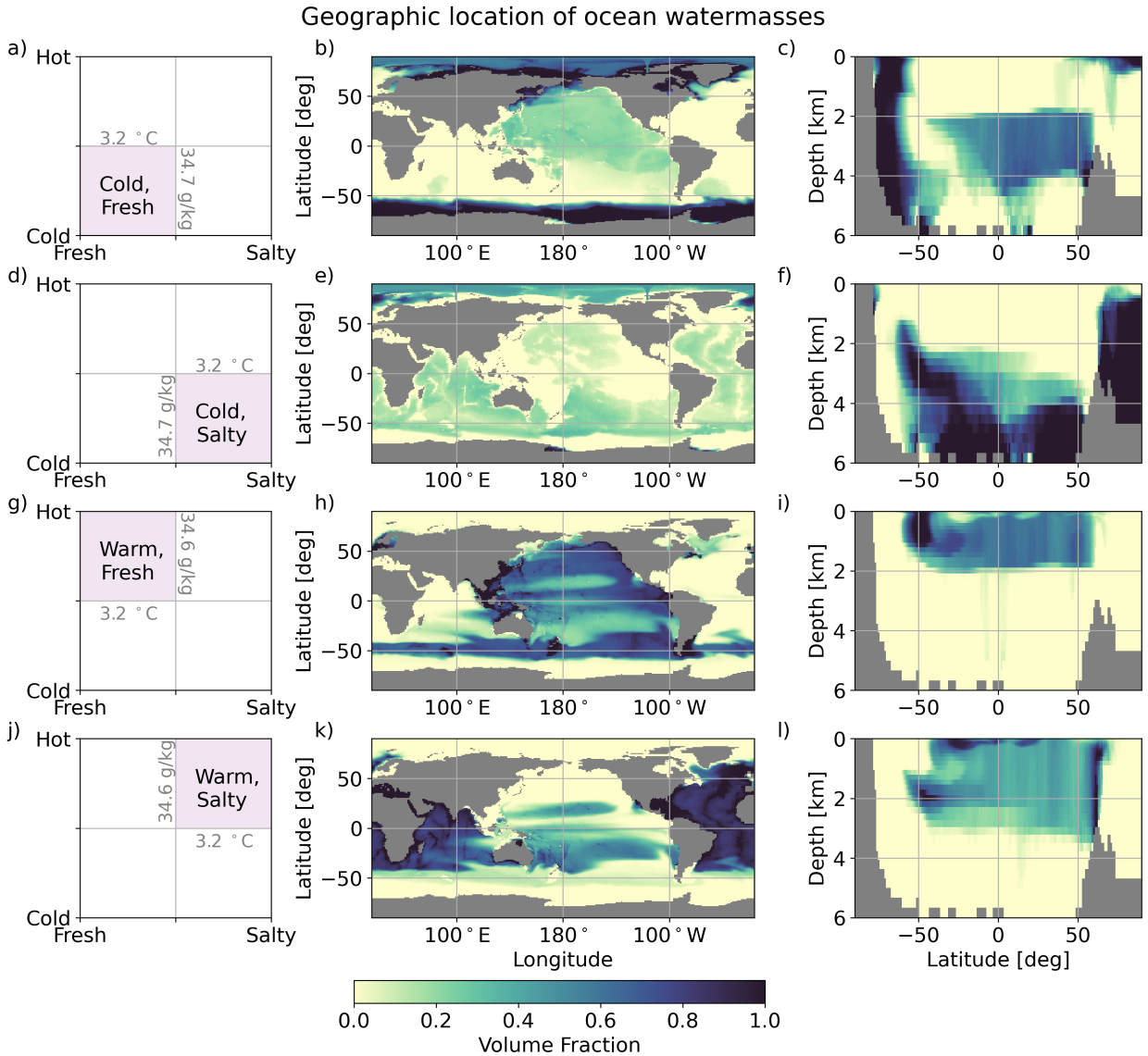
615 FIG. A1. (a and c) Median variance and (b and d) median fraction of sub-decadal variance in $T-S$ (red),
 616 latitude-longitude (blue) and latitude-depth (green) co-ordinates across 16 plausible BSP split combinations.

617 For $n = 8$, there are 16 yx and xy combinations that preserve the BSP bin aspect ratio. As the
618 variance distributions (figure 7) are highly skewed, we examine how the median (rather than mean)
619 variance changes across the 16 BSP split combinations in figure A1 a and c. For salinity, $T - S$ and
620 latitude-depth co-ordinates have extremely similar median variances across all split combinations.
621 For temperature on the other hand, latitude-depth co-ordinates have consistently lower median
622 variance than $T - S$, and this gap changes based on the specific split combination used. That said,
623 the median variance of $T - S$ and latitude-depth remains quite close relative to the latitude-longitude
624 co-ordinate system, which has a median variance that is approximately one order of magnitude
625 larger. Across all BSP split combinations, $T - S$ and latitude-depth co-ordinates are dominated by
626 multi-decadal processes, while latitude-longitude co-ordinates have a roughly equal split between
627 sub-decadal and multi-decadal processes (see figure A1 b and d). Our exploration of alternative
628 BSP split combinations further solidifies our findings, showing that our results are insensitive to
629 the order of (physically constrained) BSP splitting used.

630 APPENDIX B

631 **Geographic location of watermasses in $T - S$ space**

632 It is difficult to conceptualise changes in watermass space in terms of the geographic location of
633 said water masses. In an attempt to aid in interpretation of the results we show the volume fraction
634 in each latitude-longitude and latitude-depth grid cell that corresponds to the warmest (coldest)
635 and freshest (saltiest) 25% volume of the ocean, in figure B1. The 25% coldest and freshest ocean
636 by volume is predominantly located in the Southern Ocean and surface Arctic ocean (figure B1a,
637 b and c). Antarctic Bottom Water and Pacific subsurface waters are captured in this quadrant. The
638 25% coldest and saltiest ocean is much more broadly distributed - and largely corresponds to the
639 deepest ocean water (figure B1d, e and f). The North Atlantic Deep Water and North Atlantic
640 overturning are captured in this quadrant.



641 FIG. B1. The volume fraction, in latitude-longitude and latitude-depth co-ordinates, occupied by four water
 642 masses in $T - S$ space: (a, b and c) The coldest, freshest 25% of the ocean, (d, e and f) the coldest, saltiest 25%
 643 of the ocean, (g, h and i) the warmest, freshest 25% of the ocean and (j, k and l) the warmest, saltiest 25% of the
 644 ocean. Note that these quadrants are the same as those presented in Figure 2 for 2^2 bins, and their temperature
 645 and salinity limits are denoted in grey. Land masses are coloured in dark grey.

646 The 25% warmest and freshest ocean is largely isolated to the surface Pacific ocean, as well as
647 the Antarctic Intermediate Water, but excludes the Pacific subpolar gyres (figure B1g, h and i). The
648 25% warmest and saltiest ocean, on the other hand, is almost exclusively isolated to the Indian and
649 Atlantic oceans (excluding the Indo-Pacific warm pool), and includes the Pacific subpolar gyres
650 (figure B1j, k and l).

651 **References**

652 Allan, R. P., and Coauthors, 2020: Advances in understanding large-scale responses of the wa-
653 ter cycle to climate change. *Annals of the New York Academy of Sciences*, **1472** (1), 49–75,
654 <https://doi.org/10.1111/nyas.14337>.

655 Allison, L. C., C. D. Roberts, M. D. Palmer, L. Hermanson, R. E. Killick, N. A. Rayner, D. M. Smith,
656 and M. B. Andrews, 2019: Towards quantifying uncertainty in ocean heat content changes using
657 synthetic profiles. *Environmental Research Letters*, **14** (8), 084 037, [https://doi.org/10.1088/](https://doi.org/10.1088/1748-9326/ab2b0b)
658 [1748-9326/ab2b0b](https://doi.org/10.1088/1748-9326/ab2b0b).

659 Banks, H., R. Wood, and J. Gregory, 2002: Changes to Indian Ocean Subantarctic Mode Water in a
660 Coupled Climate Model as CO₂ Forcing Increases. *Journal of Physical Oceanography*, **32** (10),
661 2816–2827, [https://doi.org/10.1175/1520-0485\(2002\)032<2816:ctiosm>2.0.co;2](https://doi.org/10.1175/1520-0485(2002)032<2816:ctiosm>2.0.co;2).

662 Banks, H. T., R. A. Wood, J. M. Gregory, T. C. Johns, and G. S. Jones, 2000: Are observed decadal
663 changes in intermediate water masses a signature of anthropogenic climate change? *Geophysical*
664 *Research Letters*, **27** (18), 2961–2964, <https://doi.org/10.1029/2000gl011601>.

665 Bi, D., and Coauthors, 2020: Configuration and spin-up of ACCESS-CM2, the new generation
666 Australian Community Climate and Earth System Simulator Coupled Model. *Journal of Southern*
667 *Hemisphere Earth Systems Science*, <https://doi.org/10.1071/es19040>.

668 Bladwell, C., R. M. Holmes, and J. D. Zika, 2021: Internal salt content: a useful framework
669 for understanding the oceanic branch of the water cycle. *Journal of Physical Oceanography*,
670 <https://doi.org/10.1175/jpo-d-20-0212.1>.

671 Boyer, T. P., S. Levitus, J. I. Antonov, R. A. Locarnini, and H. E. Garcia, 2005: Linear trends in
672 salinity for the World Ocean, 1955–1998. *Geophysical Research Letters*, **32** (1), [https://doi.org/](https://doi.org/10.1029/2004gl021791)
673 [10.1029/2004gl021791](https://doi.org/10.1029/2004gl021791).

- 674 Durack, P. J., S. E. Wijffels, and R. J. Matear, 2012: Ocean Salinities Reveal Strong Global
675 Water Cycle Intensification During 1950 to 2000. *Science*, **336 (6080)**, 455–458, [https://doi.org/](https://doi.org/10.1126/science.1212222)
676 10.1126/science.1212222.
- 677 Evans, D. G., J. D. Zika, A. C. N. Garabato, and A. J. G. Nurser, 2014: The imprint of Southern
678 Ocean overturning on seasonal water mass variability in Drake Passage. *Journal of Geophysical*
679 *Research: Oceans*, **119 (11)**, 7987–8010, <https://doi.org/10.1002/2014jc010097>.
- 680 Eyring, V., S. Bony, G. A. Meehl, C. A. Senior, B. Stevens, R. J. Stouffer, and K. E. Taylor,
681 2016: Overview of the Coupled Model Intercomparison Project Phase 6 (CMIP6) experimental
682 design and organization. *Geoscientific Model Development*, **9 (5)**, 1937–1958, [https://doi.org/](https://doi.org/10.5194/gmd-9-1937-2016)
683 10.5194/gmd-9-1937-2016.
- 684 Griffies, S. M., and R. J. Greatbatch, 2012: Physical processes that impact the evolution of
685 global mean sea level in ocean climate models. *Ocean Modelling*, **51**, 37–72, [https://doi.org/](https://doi.org/10.1016/j.ocemod.2012.04.003)
686 10.1016/j.ocemod.2012.04.003.
- 687 Groeskamp, S., P. M. Barker, T. J. McDougall, R. P. Abernathy, and S. M. Griffies, 2019: VENM:
688 An Algorithm to Accurately Calculate Neutral Slopes and Gradients. *Journal of Advances in*
689 *Modeling Earth Systems*, **11 (7)**, 1917–1939, <https://doi.org/10.1029/2019ms001613>.
- 690 Hamlington, B. D., R. R. Leben, R. S. Nerem, and K.-Y. Kim, 2011: The Effect of Signal-to-Noise
691 Ratio on the Study of Sea Level Trends. *Journal of Climate*, **24 (5)**, 1396–1408, [https://doi.org/](https://doi.org/10.1175/2010jcli3531.1)
692 10.1175/2010jcli3531.1.
- 693 Hawkins, E., and R. Sutton, 2012: Time of emergence of climate signals. *Geophysical Research*
694 *Letters*, **39 (1)**, n/a–n/a, <https://doi.org/10.1029/2011gl050087>.
- 695 Hieronymus, M., J. Nilsson, and J. Nycander, 2014: Water Mass Transformation in Salin-
696 ity–Temperature Space. *Journal of Physical Oceanography*, **44 (9)**, 2547–2568, [https://doi.org/](https://doi.org/10.1175/jpo-d-13-0257.1)
697 10.1175/jpo-d-13-0257.1.
- 698 Hobbs, W. R., C. Roach, T. Roy, J.-B. Sallée, and N. Bindoff, 2021: Anthropogenic Temperature
699 and Salinity Changes in the Southern Ocean. *Journal of Climate*, **34 (1)**, 215–228, [https://doi.org/](https://doi.org/10.1175/jcli-d-20-0454.1)
700 10.1175/jcli-d-20-0454.1.

701 Holmes, R. M., T. Sohail, and J. D. Zika, 2022: Adiabatic and Diabatic Signatures of
702 Ocean Temperature Variability. *Journal of Climate*, **35** (5), 1459–1477, [https://doi.org/](https://doi.org/10.1175/jcli-d-21-0695.1)
703 10.1175/jcli-d-21-0695.1.

704 Holmes, R. M., J. D. Zika, and M. H. England, 2019: Diathermal Heat Transport in a Global
705 Ocean Model. *Journal of Physical Oceanography*, **49** (1), 141–161, [https://doi.org/10.1175/](https://doi.org/10.1175/jpo-d-18-0098.1)
706 jpo-d-18-0098.1.

707 Irving, D., W. Hobbs, J. Church, and J. Zika, 2020: A Mass and Energy Conservation Analysis of
708 Drift in the CMIP6 Ensemble. *Journal of Climate*, **34** (8), 3157–3170, [https://doi.org/10.1175/](https://doi.org/10.1175/jcli-d-20-0281.1)
709 jcli-d-20-0281.1.

710 Mackallah, C., and Coauthors, 2022: ACCESS datasets for CMIP6: methodology and ide-
711 alised experiments. *Journal of Southern Hemisphere Earth Systems Science*, **72** (2), 93–116,
712 <https://doi.org/10.1071/es21031>.

713 Maher, N., S. Milinski, and R. Ludwig, 2021: Large ensemble climate model simulations: in-
714 troduction, overview, and future prospects for utilising multiple types of large ensemble. *Earth*
715 *System Dynamics*, **12** (2), 401–418, <https://doi.org/10.5194/esd-12-401-2021>.

716 McDougall, T. J., 2003: Potential Enthalpy: A Conservative Oceanic Variable for Evaluating Heat
717 Content and Heat Fluxes. *Journal of Physical Oceanography*, **33** (5), 945–963, [https://doi.org/](https://doi.org/10.1175/1520-0485(2003)033<0945:peacov>2.0.co;2)
718 10.1175/1520-0485(2003)033<0945:peacov>2.0.co;2.

719 McDougall, T. J., and P. M. Barker, 2011: Getting started with TEOS---10 and the Gibbs Seawater
720 (GSW) Oceanographic Toolbox. *SCOR/IAPSO WG127*, 28.

721 Morrison, A. K., and A. M. Hogg, 2013: On the Relationship between Southern Ocean Overturning
722 and ACC Transport. *Journal of Physical Oceanography*, **43** (1), 140–148, [https://doi.org/10.](https://doi.org/10.1175/jpo-d-12-057.1)
723 1175/jpo-d-12-057.1.

724 Palmer, M. D., and K. Haines, 2009: Estimating Oceanic Heat Content Change Using Isotherms.
725 *Journal of Climate*, **22** (19), 4953–4969, <https://doi.org/10.1175/2009jcli2823.1>.

726 Palmer, M. D., K. Haines, S. F. B. Tett, and T. J. Ansell, 2007: Isolating the signal
727 of ocean global warming. *Geophysical Research Letters*, **34** (23), n/a–n/a, [https://doi.org/](https://doi.org/10.1029/2007gl031712)
728 10.1029/2007gl031712.

729 Penland, C., and L. Matrosova, 2006: Studies of El Niño and Interdecadal Variability in Tropical
730 Sea Surface Temperatures Using a Nonnormal Filter. *Journal of Climate*, <https://doi.org/https://doi.org/10.1175/JCLI3951.1>.

732 Pierce, D. W., P. J. Gleckler, T. P. Barnett, B. D. Santer, and P. J. Durack, 2012: The fingerprint
733 of human-induced changes in the ocean's salinity and temperature fields. *Geophysical Research*
734 *Letters*, **39** (21), n/a–n/a, <https://doi.org/10.1029/2012gl053389>.

735 Radha, H., M. Vetterli, and R. Leonardi, 1996: Image compression using binary space partitioning
736 trees. *IEEE Transactions on Image Processing*, **5** (12), 1610–1624, <https://doi.org/10.1109/83.544569>.

738 Rathore, S., N. L. Bindoff, H. E. Phillips, and M. Feng, 2020: Recent hemispheric asymmetry in
739 global ocean warming induced by climate change and internal variability. *Nature Communica-*
740 *tions*, **11** (1), 2008, <https://doi.org/10.1038/s41467-020-15754-3>.

741 Roemmich, D., J. Church, J. Gilson, D. Monselesan, P. Sutton, and S. Wijffels, 2015: Un-
742 abated planetary warming and its ocean structure since 2006. *Nature Climate Change*, **5** (3),
743 <https://doi.org/10.1038/nclimate2513>.

744 Schuckmann, K. v., and Coauthors, 2020: Heat stored in the Earth system: where does the energy
745 go? *Earth System Science Data*, **12** (3), 2013–2041, <https://doi.org/10.5194/essd-12-2013-2020>.

746 Silvy, Y., E. Guilyardi, J.-B. Sallée, and P. J. Durack, 2020: Human-induced changes to the global
747 ocean water masses and their time of emergence. *Nature Climate Change*, 1–7, <https://doi.org/10.1038/s41558-020-0878-x>.

749 Sohail, T., D. B. Irving, J. D. Zika, R. M. Holmes, and J. A. Church, 2021: Fifty Year Trends in
750 Global Ocean Heat Content Traced to Surface Heat Fluxes in the Sub-Polar Ocean. *Geophysical*
751 *Research Letters*, **48** (e2020GL091439), 1 – 13, <https://doi.org/10.1029/2020gl091439>.

752 Sohail, T., J. D. Zika, D. B. Irving, and J. A. Church, 2022: Observed poleward freshwater transport
753 since 1970. *Nature*, **602** (7898), 617–622, <https://doi.org/10.1038/s41586-021-04370-w>.

754 Stocker, and Coauthors, 2013: Climate Change 2013: The Physical Science Basis. Contribution
755 of Working Group I to the Fifth Assessment Report of the Intergovernmental Panel on Climate
756 Change. Tech. rep., Cambridge University Press, 1535 pp.

757 Swart, N. C., S. T. Gille, J. C. Fyfe, and N. P. Gillett, 2018: Recent Southern Ocean warming
758 and freshening driven by greenhouse gas emissions and ozone depletion. *Nature Geoscience*,
759 **11 (11)**, 836–841, <https://doi.org/10.1038/s41561-018-0226-1>.

760 Thibault, W. C., and B. F. Naylor, 1987: Set operations on polyhedra using binary space partitioning
761 trees. *ACM SIGGRAPH Computer Graphics*, **21 (4)**, 153–162, <https://doi.org/10.1145/37401.37421>.

762

763 Trenberth, K. E., 2020: ENSO in the global climate system. *El Nino Southern Oscillation in*
764 *a Changing Climate*, Vol. 253, American Geophysical Union, 21 – 37, <https://doi.org/https://doi.org/10.1002/9781119548164.ch2>.

765

766 Visbeck, M. H., J. W. Hurrell, L. Polvani, and H. M. Cullen, 2001: The North Atlantic Oscillation:
767 Past, present, and future. *Proceedings of the National Academy of Sciences*, **98 (23)**, 12 876–
768 12 877, <https://doi.org/10.1073/pnas.231391598>.

769 Walin, G., 1982: On the relation between sea-surface heat flow and thermal circulation in the
770 ocean. *Tellus*, **34 (2)**, 187–195, <https://doi.org/10.3402/tellusa.v34i2.10801>.

771 Wolfe, C. L., P. Cessi, J. L. McClean, and M. E. Maltrud, 2008: Vertical heat transport in eddying
772 ocean models. *Geophysical Research Letters*, **35 (23)**, <https://doi.org/10.1029/2008gl036138>.

773 Worthington, L. V., 1981: The Water Masses of the World Ocean:Some Results of a Fine-Scale
774 Census.

775 Zika, J. D., J. M. Gregory, E. L. McDonagh, A. Marzocchi, and L. Clément, 2021: Recent Water
776 Mass Changes Reveal Mechanisms of Ocean Warming. *Journal of Climate*, **34 (9)**, 3461–3479,
777 <https://doi.org/10.1175/jcli-d-20-0355.1>.

778 Zika, J. D., N. Skliris, A. T. Blaker, R. Marsh, A. J. G. Nurser, and S. A. Josey, 2018: Improved esti-
779 mates of water cycle change from ocean salinity: the key role of ocean warming. *Environmental*
780 *Research Letters*, **13 (7)**, 074 036, <https://doi.org/10.1088/1748-9326/aace42>.

781 Zika, J. D., N. Skliris, A. J. G. Nurser, S. A. Josey, L. Mudryk, F. Laliberté, and R. Marsh, 2015:
782 Maintenance and Broadening of the Ocean’s Salinity Distribution by the Water Cycle. *Journal*
783 *of Climate*, **28 (24)**, 9550–9560, <https://doi.org/10.1175/jcli-d-15-0273.1>.